CHALMERS
UNIVERSITY OF TECHNOLOGY

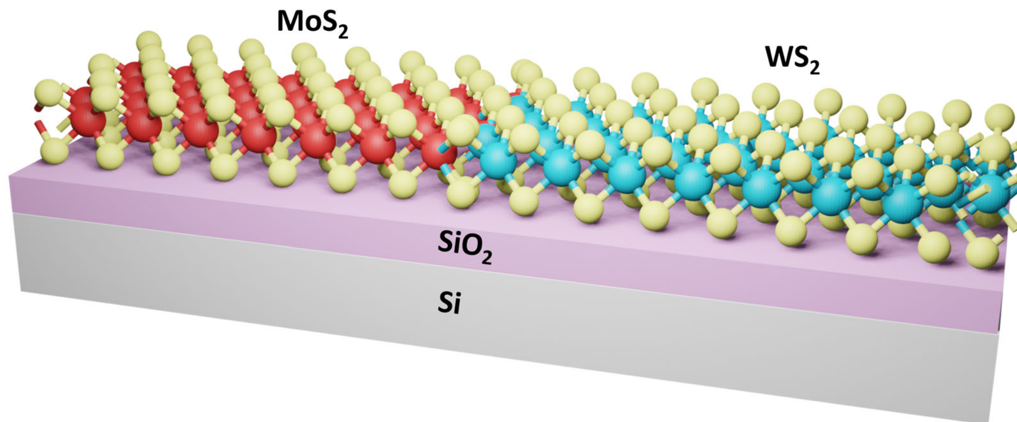

Electrical and Optoelectronic Properties of Two-Dimensional Lateral Heterostructure Semiconductors

Master's thesis in Nanotechnology

KRISHNA KUMAR BASKAR

DEPARTMENT OF MICROTECHNOLOGY AND NANOSCIENCE

CHALMERS UNIVERSITY OF TECHNOLOGY
Gothenburg, Sweden 2024
www.chalmers.se

Master's thesis 2024

Electrical and Optoelectronic Properties of Two-Dimensional Lateral Heterostructure Semiconductors

Krishna Kumar Baskar

CHALMERS
UNIVERSITY OF TECHNOLOGY

Department of Microtechnology and Nanoscience
Division of Quantum Device Physics
Chalmers University of Technology
Gothenburg, Sweden 2024

Electrical and Optoelectronic Properties of Two-Dimensional Lateral Heterostructure Semiconductors

Krishna Kumar Baskar

© Krishna Kumar Baskar, 2024.

Supervisor:
Prof. Saroj Prasad Dash, Department of Microtechnology and Nanoscience, Chalmers University of Technology
Assistant Supervisor:
Dr. Anamul Md Hoque, Department of Microtechnology and Nanoscience, Chalmers University of Technology
Examiner:
Prof. Saroj Prasad Dash, Department of Microtechnology and Nanoscience, Chalmers University of Technology

Master's Thesis 2024
Department of Microtechnology and Nanoscience
Division of Quantum Device Physics
Chalmers University of Technology
SE-412 96 Gothenburg
Telephone +46 31 772 1000

Cover: Schematic of MoS_2-WS_2 lateral heterostructure field effect transistor. The SiO_2/Si acts as a back gate. Blender software is used for the design.

Printed by Chalmers Reproservice
Gothenburg, Sweden 2024

Electrical and Optoelectronic Properties of Two-Dimensional Lateral Heterostructure Semiconductors
Krishna Kumar Baskar
Department of Microtechnology and Nanoscience
Chalmers University of Technology

Abstract

Two-Dimensional (2D) semiconductors are promising materials for atomically thin electronics and optoelectronics. Specifically, p-n junctions and their gate voltage-controlled effects in the lateral heterostructures of such 2D semiconductors offer several advantages because of their atomically thin in-plane superlattices. 2D p-n junctions have great potential for application in low-power, high-performance electro-optical devices, such as tunnel transistors, light-emitting diodes, photodetectors and photovoltaic cells. Although vertical heterojunctions are promising for electro-optical devices, the use of mechanical exfoliation process to obtain the vertical heterostructure is unsuitable for wafer-scale fabrication. The in-situ growth of high-quality lateral heterostructures with multiple junctions has just started to be explored.

In this master's thesis, we fabricated field-effect transistors (FETs) based on MoS_2-WS_2 lateral heterostructures and performed their electrical and optoelectronic characterization. The lateral heterostructures grown using the water-assisted one-pot chemical vapour deposition (CVD) are used to fabricate the back-gated FETs on Si-SiO_2 substrates with Ti/Au contacts. We characterized the individual MoS_2 and WS_2 channels and their heterojunctions. The junctions show diodic behaviour, which could be understood by the formation of n-n^+ junction. The transistor parameters are extracted for MoS_2, WS_2 and MoS_2-WS_2 heterojunction. Furthermore, we observed a persistent photoconductivity (PPC) effect with a time constant of 10 hrs at the heterojunction. The PPC effect is being explored for applications such as optoelectronic synapses, optical memory, artificial vision etc.

Keywords: Two-dimensional semiconductors MoS_2-WS_2 lateral heterostructure, back-gated field effect transistors, persistent photoconductivity effect.

Acknowledgements

I thank my supervisor Prof. Saroj Prasad Dash for his continued support and suggestions throughout my master's thesis. I sincerely thank my assistant supervisor Dr. Anamul Md Hoque for his constant guidance. I appreciate the time he has taken to share his knowledge with me. I also thank my colleagues Jonathan Blomqvist and Patrik Ullman for their timely help.

Krishna Kumar Baskar

Gothenburg, June 2024

List of Acronyms

Below is the list of acronyms that have been used throughout this thesis listed in alphabetical order:

CVD	Chemical Vapour Deposition
DFT	Density functional theory
FLP	Fermi level pinning
GAA	Gate all around
LPE	Liquid phase exfoliation
MBE	Molecular beam epitaxy
MIGS	Metal induced gap states
MOCVD	Metal oxide chemical vapour deposition
MOSFET	Metal oxide semiconductor field effect transistor
MS	Metal- semiconductor
PMMA	polymethyl methacrylate
PPC	Persistent photoconductivity
SB	Schottky barrier
SCE	Short channel effect
SS	Subthreshold swing
TLM	Transfer length method
TMD LHS	Transitional metal dichalcogenide lateral heterostructure

Contents

List of Acronyms ix

List of Figures xiii

List of Tables xv

1 Introduction 1

2 Theoretical Background and Recent Developments 4
- 2.1 Synthesis of 2D TMDs . . . 4
- 2.2 Metal contacts to 2D TMDs . . . 6
  - 2.2.1 Fundamentals of Fermi Level Pinning . . . 7
  - 2.2.2 Impacts of FLP on Device performance . . . 8
- 2.3 I-V curves of TMD Lateral Heterostructures . . . 10
- 2.4 2D TMD based photodetectors . . . 12
- 2.5 Persistent Photoconductivity (PPC) . . . 14

3 Measurement techniques 16

4 Results and Discussion 19
- 4.1 Experimental Details . . . 19
- 4.2 Electrical Characterization . . . 19
- 4.3 Schottky barrier height extraction . . . 24
- 4.4 Optoelectronic characterization . . . 27
- 4.5 Persistent Photoconductivity . . . 30

5 Summary and Conclusions 33

A Water assisted one pot CVD growth of 2D TMD LHS I

B Fabrication III

C Supplemenatry VI
- C.1 Supplementary MoS_2 and WS_2 results . . . VI
- C.2 Supplementary MoS_2-WS_2 heterojunction results . . . VII
- C.3 Supplementary SBH extraction results . . . VIII
- C.4 Supplementary photoresponse results . . . IX
- C.5 Supplementary table . . . IX

List of Figures

2.1 Illustrastion of CVD parameters influencing the 2D TMD heterostructure . . . 5
2.2 Future targets for CVD grown 2D TMDs and LHS . . . 6
2.3 Fermi level pinning of contact metals at the TMD interface . . . 9
2.4 Electrical characterization of TMD Lateral Heterojunctions . . . 11
2.5 Photodetectors based on TMD heterostructures . . . 13
2.6 Persistent Photoconductivity (PPC) effect in TMDs . . . 15

3.1 Schematic of Transfer length method (TLM) . . . 17
3.2 Basic transistor parameter extraction methods . . . 18

4.1 Electrical characterization of MoS_2 and WS_2 . . . 21
4.2 Electrical characterization of MoS_2-WS_2 lateral heterojunctions . . . 22
4.3 Temperature dependent data for MoS_2 and WS_2 . . . 23
4.4 Extraction of Schottky barrier height (SBH) . . . 26
4.5 Optoelectronic characteristics of a MoS_2-WS_2 heterojunction . . . 28
4.6 Photoinduced Schottky barrier lowering . . . 29
4.7 Experimental observation of persistent photoconductivity (PPC) . . . 32

A.1 Growth mechanism of MoS_2/WS_2 lateral heterostructure . . . II
A.2 Relative kinetic coefficient vs growth temperature and optical image of MoS_2-WS_2 LHS . . . II

B.1 Fabrication process with schematic diagrams . . . V

C.1 Supplementary MoS_2 and WS_2 results . . . VI
C.2 Supplementary MoS_2-WS_2 heterojunction results . . . VII
C.3 Supplementary SBH extraction results . . . VIII
C.4 Supplementary photoresponse results . . . IX

List of Tables

C.1 Basic transistor parameters of MoS_2 in pristine, annealed and laser illuminated conditions . . . IX
C.2 Basic transistor parameters of MoS_2-WS_2 Heterojunction in pristine, annealed and laser illuminated conditions . . . X
C.3 Basic transistor parameters of WS_2 in pristine, annealed and laser illuminated conditions . . . X

1
Introduction

Transistors play a pivotal role in the development of modern microelectronics. In logic applications, the metal-oxide-semiconductor field effect transistor (MOSFET), an electronic switch, is the fundamental unit of integrated circuits. For the last six decades, vigorous MOSFET scaling has taken place. Scaling down of MOSFETs will not only increase the density of transistors but also increase the frequency response and reduce the switching energy [1]. However, MOSFET size scaling leads to short-channel effects (SCE) which severely affect the transport of electrons in the channel and the electrostatics of the MOSFET. In short-channels, the congested inversion layer sheet carriers at the oxide-semiconductor interface at high gate overdrive enhance the interface roughness scattering and phonon scattering which results in severe carrier mobility degradation [2].

Besides mobility degradation, the scaling of MOSFETs has undesirable effects such as threshold voltage (V_T) roll-off, drain-induced barrier lowering (DIBL), and degradation of subthreshold swing (SS) due to the dominance of drain electrostatics on the channel charges. To avoid these SCE, MOSFET has undergone various device design changes in the last 50 years such as the introduction of high-k dielectric (Hafmium Oxide (HfO_2)) [3] and strained channels [4] to improve the performance of MOSFET and keep the trend of Moore's law. To further decrease the gate length with improved channel electrostatics and reduced electrostatic length, FinFET architecture was introduced at the 22nm technology node. However, scaling fin width below 5 nm results in performance degradation due to fin width variability [5]. Gate all around (GAA) FET is being explored with nanosheets and nanowires for beyond FinFET technology [6]. However, confining the channel into a two-dimensional (2D) layer will result in an energy band splitting and reduce the inversion layer capacitance. Silicon (Si) channel experiences significant mobility degradation due to surface roughness scattering below 4nm thickness [7]. Therefore, it's challenging to scale Si thickness beyond 4nm without mobility degradation and bandgap enhancement. Further gate length scaling and better control over off-state leakage require thinner body channel materials with high carrier mobility.

Atomically thin, dangling bond-free 2D layered transition-metal dichalcogenides (TMDs) are extremely promising channel materials for atomically thin transistors because they retain their carrier mobilities down to monolayer thicknesses less than 1 nm. Although graphene shows high mobility, the zero bandgap results in a significant off-state current. 2D materials have initiated numerous research efforts in developing novel electronic devices and design architectures. Among TMDs, MoS_2,

$MoSe_2$, WS_2, and WSe_2 based devices are extensively investigated because of their large band gap and high mobility. [8] [9]

2D materials are also promising candidates for ultrathin photodetectors [10]. A photodetector is an optoelectronic device used to convert light signals into electrical signals. High-performance photodetectors have various applications including optical communication, electro-optical displays, biomedical imaging, environmental monitoring etc [11]. Graphene-based photodetectors show a fast photoresponse time, and wider bandwidth in the range of GHz. However, the semimetal nature of graphene leads to high dark current which prevents their use as photoabsorbers. 2D TMDs and their heterostructures are good choices for photodetectors because of their strong light-matter interaction and broadband photoresponse. Monolayer TMDs with a direct bandgap in the range of 1-2.5 eV are being investigated for visible and near-infrared photodetectors [12].

The integration of TMD lateral heterostructure offers several advantages over single TMDs for optoelectronic applications: (1) optimization of band alignment (2) efficient production, confinement and transport of photogenerated carriers due to dangling bond-free interface (3) advantage of combining different TMD materials to achieve a wide range of photodetection spectrum [11]. Recently, photodetectors based on 2D TMD lateral heterostructure exhibited ultrahigh photoresponsivity and specific detectivity, much higher than single 2D TMDs [13]. These excellent performances render 2D TMD lateral heterostructures promising candidates for photodetectors.

Recently, Persistent Photoconductivity (PPC) has been observed in 2D TMDs with time-constant ranging from a few seconds to several days [14] [15]. PPC is an optoelectronic phenomenon, in which the photoconductivity persists even after the termination of the light source. The PPC effect has been explored for applications such as optoelectronic synapses, optical memory, artificial vision etc. The optoelectronic memory has been demonstrated with the gate tunable PPC effect in MoS_2 phototransistors [16]. So far, the demonstration of the PPC effect is only limited to single TMDS such as MoS_2, WS_2, $MoSe_2$, and WSe_2.

In this master's thesis, we have fabricated back-gated field effect transistors (FETs) based on MoS_2-WS_2 lateral heterostructures and performed the electrical and optoelectronic characterization. The lateral heterostructures grown using the water-assisted one-pot CVD method are used to fabricate the devices. Transfer length method (TLM) analysis is performed for MoS_2. The Schottky barrier height (SBH) of MoS_2 and WS_2 are extracted using a back-to-back diode model. The photoresponsivity and gain factor at the heterojunction are calculated. We also demonstrated the PPC effect at the MoS_2-WS_2 heterojunction.

The master thesis is organised as follows: Chapter 2 discusses the theoretical background and the state-of-the-art challenges in the field of 2D TMDs. Topics such as synthesis of 2D TMDs heterostructure, contact engineering, photodetectors based on TMDs, and PPC phenomenon in TMDs are discussed in detail. Electrical measurement techniques used for the transistor characterization are discussed briefly in

Chapter 3. Chapter 4 focuses on the electrical and optoelectronic characterization of MoS_2-WS_2 heterostructure. Results of temperature-dependent measurements, Schottky barrier extraction, photoresponse and PPC effect are presented and discussed. Device fabrication processes and material characterization are also explained at the beginning of this chapter. A detailed description of the water-assisted one-pot CVD method and the device fabrication processes are given in Appendix A and Appendix B respectively. Supplementary data are given in Appendix C.

2

Theoretical Background and Recent Developments

2D TMDs have been extensively explored as channel materials for low-power electronics, because of their dangling bond-free van der Waals surface and atomic level thickness. The suppressed short-channel effects, absence of gap states at interfaces, and good electrostatic control of 2D TMDs make them promising for scaled field-effect transistors. However, the pathway of 2D TMDs and their heterostructures is still in a nascent stage and poses numerous challenges including, difficulties of low thermal budget synthesis of wafer-scale single-crystalline of 2D TMDs, and low carrier mobilities. In this section, a comprehensive overview of the theoretical background and the state-of-the-art challenges in the synthesis of 2D TMDs lateral heterostructures, metal contact engineering, and 2D TMDs-based photodetectors are discussed.

2.1 Synthesis of 2D TMDs

The lateral heterostructures (LHS) of 2D TMDs will enable the fabrication of in-plane diodes and transistors. Unlike vertical heterostructures, LHS cannot be synthesized through the exfoliation method and therefore direct synthesis is the only way to grow lateral heterojunction. Large-scale direct growth of LHS with controlled domain size, orientation, layer number and clean and atomically sharp interface is necessary [17]. The CVD method is generally used to synthesize heterostructure compared to MOCVD and MBE.

Huang et al. synthesized the first CVD-grown LHS of monolayer $MoSe_2$–WSe_2 using a heterogenous mixture of bulk powders ($MoSe_2$–WSe_2) as a source precursor [18]. In this method, the precursor is heated to 950°C and H_2 is used as a carrier gas. The change in the vapour pressure of the precursor led to the formation of LHS. However, through this method, multijunction heterostructures cannot be realized. The in situ source transfer CVD method is developed by Duan et al. to synthesize WS_2-WSe_2 LHS. In this method, after the initial synthesis of WS_2, the source precursor is taken out of the hot chamber and replaced with the WSe_2 precursor [19]. The unsaturated dangling bonds at the edges of the WS_2 triangular films act as a nucleation site for the growth of WSe_2. Zhang et al. developed a lateral TMD multijunction which requires the exchange of a CVD growth chamber for the growth of each individual TMD domain [20]. However, since the TMDs are very sensitive

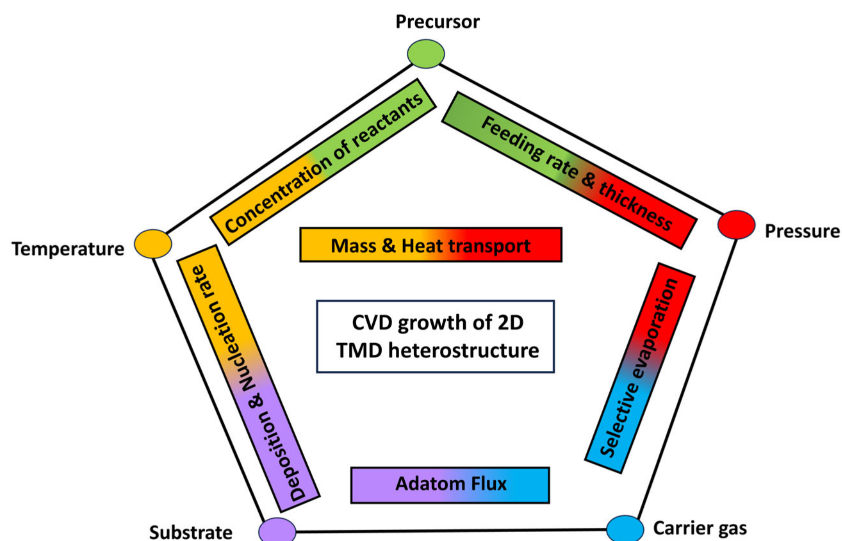

Figure 2.1: : Illustration representing how different parameters influence the thermodynamic and kinetic factors during the CVD growth of TMD domains. The illustration is adapted from [17].

to minute variations in growth conditions such as vapour pressure and temperature, the unsaturated dangling bonds can be passivated by reacting with other chemical or gaseous reagents. These sequential exposures to the laboratory environment lead to the formation of alloys at the heterojunction interface and lack of long-range ordering [21].

To overcome the limitations of the sequential multijunction LHS fabrication, Sahoo et al. has developed a water-assisted one-pot synthesis method [22, 23]. In this method, heterogenous TMD bulk powders (MoS_2/WS_2) are used as a precursor and carrier gas is changed to promote selective vaporization and growth of TMD. The carrier gas, N_2 + H_2O(g) promotes the vaporization of Mo-related precursors and results in the nucleation of MoX_2 domains. When the carrier is changed to H_2 + Ar, W precursor will get vaporized and WX_2 domains will start nucleating by terminating the growth of MoX_2. Through the sequential exchange of carrier gas, multijunction heterostructure is realized. In this master's thesis, TMD LHS grown using this method is used to fabricate the back-gated field effect transistors (FETs). More details about the growth mechanisms and conditions are explained in Appendix A.

Though novel electronics and optoelectronics are being developed using 2D TMD-based LHS, there are many challenges that need to be addressed prior to real-world applications. To date, the size of LHS is limited to μm and requires transferring to the target substrate. For large-scale applications, direct growth of wafer-scale single-crystalline 2D LHS is required. Also, further understanding of the growth mechanism is required to get precise control over grain size, thickness, grain orientation, defects, and morphology of LHS. Furthermore, it's essential to fabricate devices based on LHS with low thermal budget, high reproducibility, spatial uniformity and

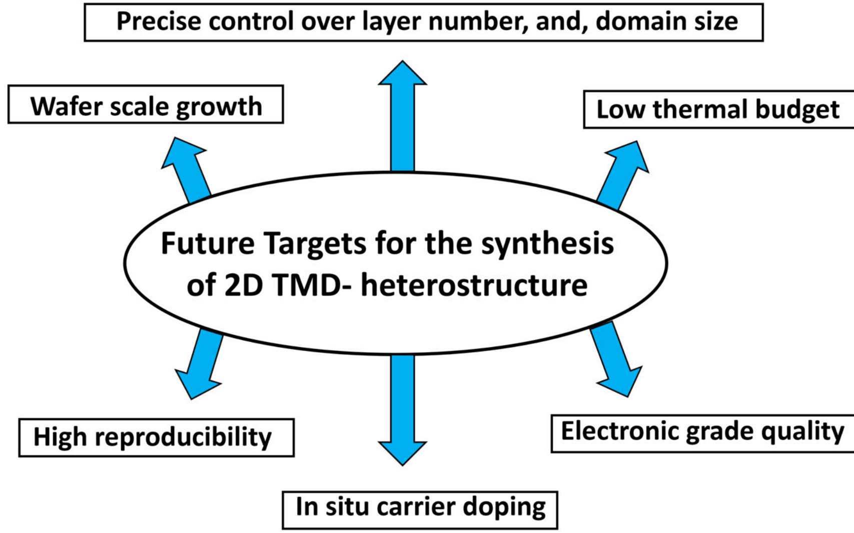

Figure 2.2: Future targets for the state-of-the-art CVD grown 2D TMDs and LHS.

temporal uniformity. Figure 2.2 shows the future targets of the CVD-grown 2D TMDs heterostructure.

2.2 Metal contacts to 2D TMDs

In principle, 2D TMDs should have vdW interaction with metal. However, covalent bonding is observed at metal- 2D material interfaces. This leads to a strong Fermi level pinning (FLP), which results in Schottky barrier height (SBH). The FLP and SBH are the main reasons for large contact resistance (R_c) and low carrier charge mobilities observed in 2D TMDs. In Si-based transistors, this problem is circumvented by heavy doping. The substitutional doping techniques used in Si MOSFETs to achieve ohmic contacts, such as ion implantation and thermal diffusion, cannot be employed in 2D TMDs, because of the introduction of surface defects and destruction of crystals lattice by the energetic ions.

The absence of such doping methods necessitates the use of suitable contact metals for efficient carrier injection into the channels to achieve low contact resistance. When a contact metal of work function ϕ_m is deposited on a 2D TMD channel having electron affinity χ_s, Schottky barriers (SB) are formed with SB height given by Schottky-Mott rule:

$$\phi_{SB-n} = \phi_M - \chi_s \tag{2.1}$$

$$\phi_{SB-p} = E_G + \chi_s - \phi_M \tag{2.2}$$

Where, E_g is the bandgap of the TMD channel and ϕ_{SB-n}, ϕ_{SB-p} are the SB heights for electrons and holes respectively. A low work-function metal with the fermi level

near the semiconductor conduction band will improve the electron injection whereas a high work-function metal will facilitate hole injection. Only in an ideal metal-semiconductor (MS) interface, the Schottky-Mott rule will be followed. However, in practical devices, the Schottky-Mott rule does not agree with the experimental data due to the presence of interface gap states. These interface states act like donor atoms below the charge neutrality level (E_{CNL}) and acceptor atoms above the E_{CNL}. The distribution of these electronic states within the semiconductor band gap at the MS interface leads to fermi-level pinning (FLP). When the density of gap states is infinite, the metal fermi level gets pinned at the interface charge neutrality position and this limit is called as Bardeen limit. This leads to a weaker dependency of SB height on contact metal work function and causes severe deviation from the Schottky-Mott rule. With the inclusion of the FLP phenomenon, the actual SB height is given by Eq (2.3), where S is the pinning factor and ϕ_{IS} represents the interface charge neutrality position.

$$\phi_{SB-n} = (s \times \phi - \chi_S) + (1 - s)\phi_{IS}, \qquad S = \partial\phi_{SB-n}/\phi_M \tag{2.3}$$

It varies between S=0, for strong pinning (Bardeen limit) to S= 1 for weak pinning (Schottky limit). The pinning factor, S is related to the interface gap state density N by

$$S = \frac{1}{1 + \frac{N\delta e}{\varepsilon\varepsilon_o}} \tag{2.4}$$

where δ and $\varepsilon\varepsilon_o$ represent the decay length of the states and dielectric constant around the interface. In an ideal metal-TMD contact, a vdW gap that exists acts as a tunnelling barrier for carrier injection. However, in practical TMD FET devices disorder gap states, strong metal TMD hybridization and work function modification can occur at the interface, which results in FLP.

2.2.1 Fundamentals of Fermi Level Pinning

Due to the atomic level thinness of 2D TMDs, the surfaces get easily damaged resulting in interface gap states. Interface gap states such as metal-induced gap states (MIGS) and disorder-induced gap states (DIGS) are often observed in 2D TMDs. FLP has been observed in 2D TMDs and from the theoretical and experimental investigations several conjectures were made about the origin of FLP:

1. **Intrinsic contributors:** Due to the strong chemical bonding between the chalcogen atoms and the contact metal atoms, the metal electron wave function can penetrate the 2D TMD and create MIGS, which results in FLP. Another intrinsic contributor apart from MIGS is the interface dipole caused by the electron exchange between TMDs defect states and the substrate Fermi level [24]. The interface dipoles alter the energy band alignment at the MS interface and make the fermi level pin near the conduction band edge. Furthermore,

the metalwork function gets modified severely due to the presence of a charge depletion region. MIGS and interface dipoles are believed to be the main contributors to FLP in 2D TMDs Even in a defect-free interface, it is observed that the metal fermi level is strongly pinned with a pinning factor of around S=0.3 due to MIGS and interface dipoles [25].

2. **Extrinsic contributors:** The presence of structural defects strengthens the FLP by creating DIGS. Structural defects are classified based on their dimensionalities as 0D (vacancies, adatoms, substitutional), 1D (line vacancies, passivation of edges, grain boundaries), and 2D (heterolayer stacking, wrinkling, folding, rippling). It is observed that the pinning factor gets reduced by 40% due to DIGS compared to pristine surface [26]. High concentrations of sulfur vacancies, which can act as electron donors within the bandgap are responsible for strong FLP. In MoS_2, S vacancies are formed spontaneously due to low formation energy [27]. The agglomeration of sulfur vacancies during electron bombardment results in an extrinsic sulfur line vacancy. Line vacancies along the zig-zag direction are predominant because of the low formation energy. Ripples, folding, and wrinkles are also common 2D structural defects observed during the growth and transfer process. The thermal expansion coefficient mismatch between TMD and substrate results in the formation of ripples [28]. Structural defects such as grain boundaries, vacancies, and substitutional doping are unintentionally generated due to the fluctuating growth conditions during the CVD method.

2.2.2 Impacts of FLP on Device performance

FLP in TMDs often leads to high contact resistance and unipolarity characteristics of transistors. The large SB height and width, which prevent efficient injection of carriers from the contact metal into the TMD channel, are responsible for high contact resistance [29]. Since the SB height deviates much from the Schottky-mott rule due to strong FLP, the polarity (n-type and p-type) of transistors is often unadjustable.

1. **High contact resistance:** In Schottky contacts, the contact resistivity depends on the Schottky barrier height (ϕ_{BH}) and doping at the interface (N) as given by the following equation

$$\rho_c \propto exp\left(\frac{2\phi_B}{\hbar}\sqrt{\frac{\varepsilon_s m^*}{N}}\right) \tag{2.5}$$

The contact resistivity can be reduced by either increasing the doping concentration or decreasing the SB height. Ohmic contacts with contact resistance below 0.1 k$\Omega\mu$m is required for low-power consumption transistors. However, due to strong FLP and lack of doping methods in 2D TMDs, realizing low contact resistance and ohmic contacts is a major challenge. Even for low-work

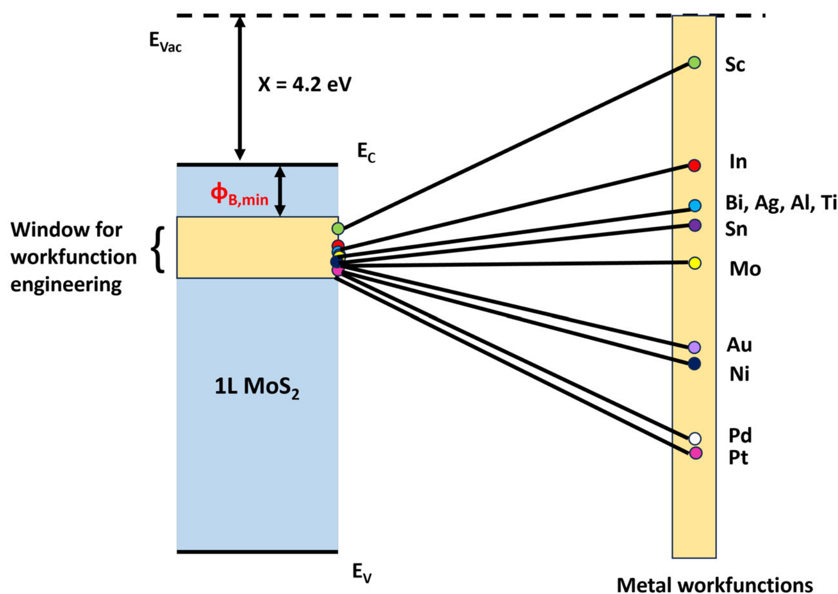

Figure 2.3: Band diagram of a monolayer MoS_2 with fermi level pinning of contact metals at the interface. For wide-ranging metals with work functions ranging from 3.4 eV to 5.9 eV, the fermi level is pinned onto a narrow energy band near the conduction band edge. Therefore, n-type polarity is often achieved in 2D TMDs.

function metal such as Sc, ohmic contact has not been achieved. For TMDs, contact resistance of 10-10^4 k$\Omega\mu$m has been commonly observed. There are several issues with device performance due to large contact resistance. The effective mobility is significantly reduced due to large voltage drops at the contact interface. Since the Schottky barrier influences the on-state characteristics and device switching, weak gate tunability is observed at short channels.

2. **Unipolarity of 2D TMD transistors** In MoS_2, the FLP pins near the conduction band edge with a low pinning factor of 0.01 which often results in n-type transistor characteristics for different contact metals with work function varying from 3.5 to 5.9 eV [30]. Figure 2.5 illustrates that for wide-ranging contact metals, the fermi level is pinned to a narrow energy band near the conduction band edge for monolayer MoS_2. In MoS_2, the SB height for electrons is much lower than for holes and this always leads to n-type transistor characteristics regardless of metals with high work function. This unadjustable polarity in MoS_2 prevents the realization of complementary logic devices that require both n-type and p-type characteristics. For WSe_2, the FLP is near the middle of the band gap and thus makes the hole injection easier compared to MoS_2. However, the ON state current is low due to less efficient hole injection through SB [31]. Although WSe_2 is a better choice for p-type 2D TMD FETs, still the MS interface must be improved to reduce the contact resistance. By optimizing the metal deposition technique, defect-free van der Waals contact between WSe_2 and Pd has been achieved recently [32].

2.3 I-V curves of TMD Lateral Heterostructures

Several authors have reported diode-like responses of the TMD lateral heterojunctions that are useful in optoelectronic device applications. However, control over the polarity of the transfer behavior of the TMD domain remains challenging.

Sahoo et al. demonstrated a diode-like response across the $MoSe_2$-WSe_2 heterojunction [22]. The water-assisted one-pot CVD-grown lateral heterostructure was used to fabricate the devices. Figure 2.4 (a)-(i) shows the optical image of the fabricated $MoSe_2$-WSe_2 heterostructure field-effect transistor. As seen from the figure 2.4 (a)-(ii), $MoSe_2$ and WSe_2 shows p-type and n-type transfer characteristics. The $MoSe_2$ domain is electron-doped whereas the WSe_2 domain is hole-doped. This difference in the doping level results causes the energy band to bend at the heterojunction. Figure 2.4 (a)-(iii) indicates that the lateral heterojunction displays diode-like behaviour/p-n junctions.

Liu et al. reported n-type rectifying characteristics of a lateral bilayer MoS_2-WS_2 heterojunction [13]. Figure 2.4 (b)-(i) shows the schematic diagram of the fabricated device. The lateral heterojunction showed a diode-like response with a current ratio of 10^3. Figure 2.4 (b)-(ii) shows the output characteristic curve of the heterojunction. Figure 2.4 (b)-(iii) shows the transfer curve of the heterojunction. The inset illustrates the energy band diagram at the heterojunction. Since both MoS_2 and WS_2 showed n-type transfer behavior, the heterojunction is n-n^+ doped.

The amount of doping level in the TMD domains determines the polarity of the transfer curve. The structural defects incorporated during the CVD growth process such as chalcogen vacancies alter the doping level.

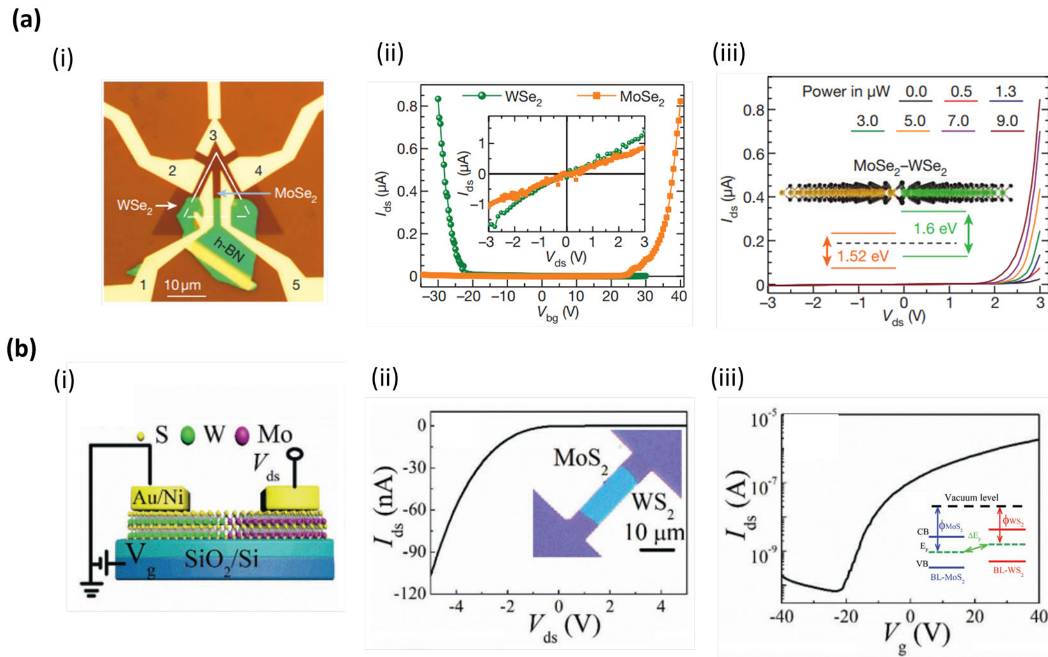

Figure 2.4: Electrical characterization of TMD Lateral Heterojunctions: (a)-(i) Optical image of the CVD grown $MoSe_2$-WSe_2 heterostructure field-effect transistor.(ii) Transfer characteristics of $MoSe_2$ and WSe_2 showing n-type and p-type behavior respectively. The inset shows the output characteristic curves. (iii) Diode-like behavior of the heterojunction. (b)-(i) Schematic diagram of the Lateral bilayer MoS_2-WS_2 heterostructure device configuration (ii) Output characteristic curve of heterojunction showing rectifying behavior. (iii) Transfer characteristic curve of the MoS_2-WS_2 heterojunction. The inset shows the energy band diagram of the heterostructure. The figures from (a) and(b) are adapted from [22] and [13] respectively.

2.4 2D TMD based photodetectors

2D TMD heterostructures are promising materials for photodetectors because of their high photoresponsivity, high bandwidth, and fast response speed. Excellent optoelectronic performances have been reported for p-n junction 2D TMD heterostructures-based photodetectors. The p-n junction is important for the photodetection mechanism and is widely used in various applications such as photosensors, LED, and photovoltaic cells. Vertical and lateral TMD/TMD heterostructures have shown promising results.Several authors have reported TMD-based photodetectors with promising results.

Li et al. demonstrated a photodetector based on MoS_2/WS_2 lateral heterostructure grown using a one-step liquid phase CVD method (figure 2.5 (a)) [33]. The heterostructure shows a photoresponsivity of 570 A/W and detectivtivity in the order of 10^{11}. The observed longer response time (rise and fall time) is attributed to the photogatong effect. The charge impurities and trapping sites present in the heterostructure resulted in a high 1/f noise.

Caeri et al. have developed a WS_2/MoS_2 heterobilayers grown using a pulse laser deposition (PLD) and demonstrated a photodetector with an ultrahigh responsivity of 2.5×10^{5} AW^{-1}, detectivity of 4.2×10^{14} Jones at 405 nm excitation (figure 2.5 (b)) [34]. The heterojunction showed an on-off ratio in the order of 10^5.

Alkesh et al. demonstrated a photodetector based on $MoSe_2/WSe_2$ heterostructure with enhanced absorption in the visible region and 1.5 times improved performance than WSe_2. The in-situ measurement at the heterointerface revealed a staggered band alignment. The heterojunction exhibited a responsivity of 1.03mA/W at 560 nm excitation (figure 2.5 (c)) [35].

Outstandingly performing photodetector based on lateral bilayer MoS_2-WS_2 heterostructure has been reported by Yongjun Tian et al[13]. The heterostructure showed a high photoresponsivity and detectivity of 6.7×10^{3} AW^{-1} and 3.1×10^{3} AW^{-1} respectively for 457 nm laser excitation. The photodetector performed much better than single TMDs (MoS_2, and WS_2). The MoS_2 and WS_2 showed n-type and p-type characteristics behaviour. The heterojunction exhibited a rectifying ratio of 10^3 with current flowing from WS_2 to MoS_2.

Wang et al. for the first time reported an infrared light photodetector based on WS_2/MoS_2 vertical heterostructure [36]. Although MoS_2 and WS_2 are insensitive to the infrared light, the MoS_2-WS_2 heterojunction showed a good response to infrared. The interlayer coupling at the heterojunction shrinks the energy gap which eventually makes the heterostructure respond to longer wavelengths. The infrared light absorption is further enhanced by incorporating gold nanoparticles. The surface plasmon resonance phenomenon in Au nanoparticles enhanced the photoresponsivity by 25 times.

Although photodetectors based on TMD heterostructure shows encouraging results, there is still much improvement needed to realize the full potential of the material

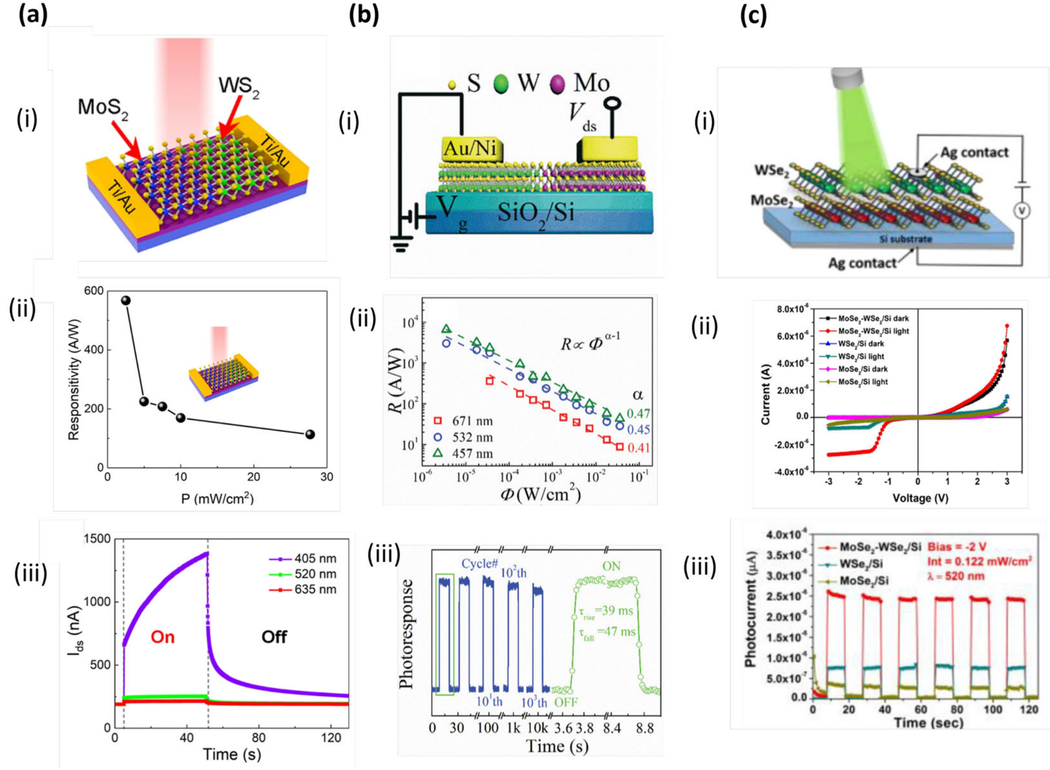

Figure 2.5: Photodetectors based on TMD heterostructures:(a)- (i) Schematic diagram of MoS_2-WS_2 photodetector. (ii) Dependence of responsivity on laser power density. (iii) Photoswitching characteristics. Figures are adapted from [33].(b) (i) Schematic diagram of the Laeral bilayer MoS_2-WS_2 heterostructure device configuration (ii) Responsivity as a function of the incident laser power density. (iii) Temporal responses of the photodetector. Figures are adapted from [34].(c) (i)Schematic diagram of $MoSe_2$-WSe_2 heterojunction, (ii) Output characteristic curves under dark and illumination. (iii) Transient photoresponse. Figures are adapted from [35].

and find potential application. The ultrathinness of 2D TMDs often limits the external quantum efficiency and detectivity due to insufficient light absorption. The high photoresponsiity reported in 2D TMD photodetectors is because of the longer carrier life time which often results in large response speed. In most of the TMD photodetectors, large generation-recombination (G-R) noise is observed due to the prolonged carrier life time which limits the detectivity of the photodetector. Therefore, TMD photodetectors with detectivity greater than 10 ^{12} Jones and response time in the range of μ sec are required. The most important challenge is the growth of large-scale high-quality homogenous 2D TMD heterostructures. It's observed that the heterointerface with structural defects results in a longer carrier lifetime.

2.5 Persistent Photoconductivity (PPC)

Persistent Photoconductivity (PPC) is a mechanism in which the photoconductivity persists for some time after the termination of light excitation. PPC phenomenon has been observed in 2D TMDs such as MoS_2, and $MoSe_2$. Recently, the PPC effect has been explored for a wide range of applications such as optoelectronic synapse, optoelectronic memory, artificial vision, and solar cells [37, 38]. The origin of the PPC phenomenon has been explained through various models such as Random Local Potential Fluctuation Model (RLPF), Macroscopic Barrier Model (MB), and Large Lattice Relaxation Model(LLR) [39, 40, 41]. The RLPF model is often used to explain the observed PPC in TMDs. However, what causes the potential fluctuations is still unclear. Several authors have observed PPC in various TMD materials and have tried to explain the origins of the PPC effect.

Wu et al. analyzed the effect of substrate on the PPC effect in monolayer MoS_2 [14]. Figure 2.6 (a) shows the schematic diagram of the device and the photoresponse of the substrate supported and suspended MoS_2. The suspended sample showed negligible PPC, whereas the substrate supported MoS_2 exhibited significant PPC. This clearly shows that the extrinsic defects from the substrate such as surface adsorbants, and substrate non-uniformity causes the PPC effect. This finding signifies the importance of the extrinsic defects on the PPC.

A giant persistent photoconductivity (GPPC) effect has been reported by George et al. in a monolayer MoS_2 (figure 2.6 (b)) [15]. The decay of the photocurrent exhibited a time constant of around 30 days at room temperature. The author concluded that the GPPC effect arises due to the spacial potential fluctuations near band edges caused by structural defects of TMDs such as atomic vacancies. Scanning tunnelling microscope and transmission electron microscope characterization are done to corroborate the results.

Bartolomeo et al. observed the PPC effect in monolayer MoS_2 with a time constant of 300 sec [42]. The author attributed the PPC effect to the photogating effect caused by the charge trapping at the SiO_2-MoS_2 interface and due to random potential fluctuations arising from the structural defects on the surface of Mos_2.

PPC effect has also been observed in a CVD grown and stacked $MoSe_2$-$Mo_{1-X}W_xSe_2$ vertical heterostructure [43]. Figure 2.6 (c) shows the optical image of the vertical heterojunction and decay of photocurrent. The photoconductivity persists for few days with a decay time constant of 12.2 hrs at room temperature.

In conclusion, both the extrinsic (substrate defects, SiO_2-TMD interface) and intrinsic defects (atomic vacancies), cause PPC phenomenon in 2D TMDs and heterostructure.

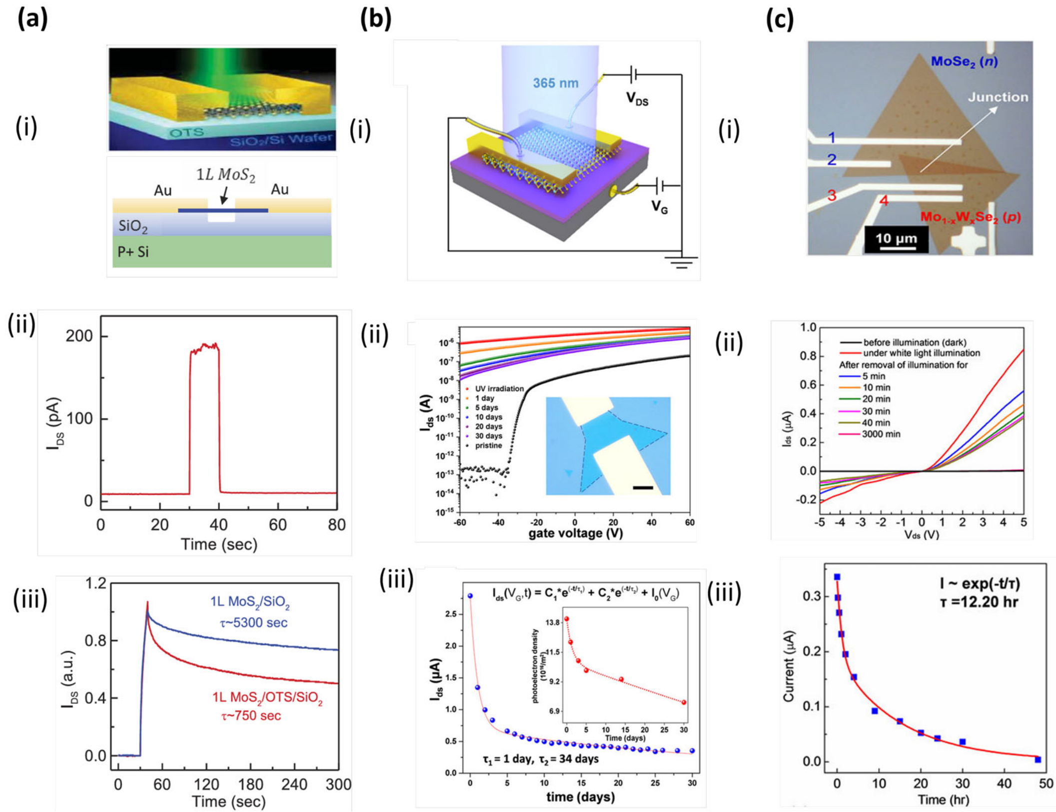

Figure 2.6: Persistent Photoconductivity (PPC) effect in TMDs:(a) (i) Schematic diagram of substrate supported and suspended MoS_2. (ii) Photoresponse of the suspended MoS_2 exhibiting negligible PPC effect. (iii) Photoresponse of the substrate supported MoS_2 showing significant PPC effect. Figures are adapted from [14]. (b) (I) Schematic of MoS_2 device with the experimental setup. (ii) Comparison of transfer characteristics curve before and after UV irradiation. (iii) Drain current decay showing giant persistent photoconductivity (GPPC) with time constants of 34 days. Figures are adapted from [15].(c) (i) Optical image of the $MoSe_2$-$Mo_{1-X}W_xSe_2$ heterostructure.(ii) Output characteristic curve of the heterojunction before and after illumination. (iii) Photoresponse after removal of light showing PPC effect with a time constant of 12.2 hrs. Figures are adapted from [43].

3

Measurement techniques

To assess the electrical performance of the TMD FETs, we extracted carrier mobility, threshold voltage, subthreshold swing (SS), drain-induced barrier lowering (DIBL), I_{max}/I_{min} ratio, contact resistances (R_C), channel sheet resistances (R_{Sh}) and Schottky barrier height (SBH). The transfer length method (TLM) is used to find the R_C and R_{Sh}. We measured the photoresposivity and gain factor from the photocurrent to perform the optoelectronic characterisation. In this section, how the parameters mentioned above are extracted from the transfer characteristics curves is briefly explained.
The TLM structure, developed by H.H. Berger in 1972 [44] is widely used to determine the contact resistance between semiconductor and metal. TLM structure consists of several FETs with varying channel lengths as shown in figure 3.1(a). The total resistance of 2D FET depends on the contact resistance (R_C), the channel sheet resistance (R_{sh}), the channel length (L_{ch}) and width (W) as shown in the following equation.

$$R_{tot} = 2R_c + R_{Sh} \cdot \left(\frac{L_{Ch}}{W}\right) \tag{3.1}$$

Using TLM structure, the R_{tot} is determined from the transistors and plotted as a function of L_{ch} as shown in figure 3.1 (b). The y-intercept of the plot gives the sum of the source and the drain contact resistances and the slope gives the channel sheet resistance. In this master's thesis, TLM structure is fabricated on MoS_2 with channel lengths varying from 0.52 μm to 1.5 μm. Resistances normalized by channel width are reported. Although TLM analysis is widely used, the presence of large error bars in contact resistance due to poor TLM design is a main disadvantage. The error bars in contact resistance can be minimized by decreasing the channel lengths. Fabricating a TLM with shorter channel lengths would reduce the confidence interval bandwidth at $L_{ch} = 0$ μm. This would significantly decrease the stand error in R_C.

Depending on the extraction method, there are two types of carrier mobility : (a) effective mobility and field-effect mobility. The effective mobility is extracted from the linear regime of the output characteristic curve whereas the field-effect mobility is extracted from the transfer characteristics curves in the linear regime. Since the output characteristics curve of our sample did not show a linear dependence on V_{ds}, the effective mobility gives erroneous values. Therefore, field-effect mobility is used in this thesis to assess the electrical performance of the transistors.

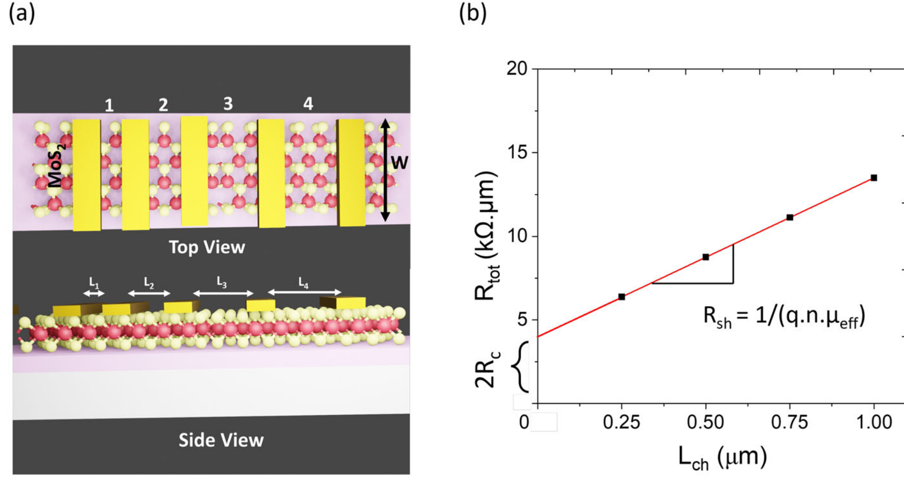

Figure 3.1: Transfer length method: (a) Schematic of TLM structure on monolayer-MoS_2 with 4 FETs of varying channel length. The top view and side view are shown. (b) Plot showing the dependence of total resistance (R_{tot}) on channel length (L_{ch}). The contact resistance (R_C) and sheet resistance (R_{sh}) are determined from the y-intercept and slope of the plot.

The field-effect mobility is extracted by calculating the average transconductance (g_m) in the linear regime of the transfer curves as shown in figure 3.2 (a). The following equation is used to calculate the mobility.

$$\mu = \left(\frac{dI_{ds}}{dV_{gs}}\right) \cdot \left(\frac{L_{ch}}{W_{ch}.C_{ox}.V_D}\right) \tag{3.2}$$

where L_{ch}, W_{ch} and C_{ox} are the channel length, channel width and capacitance per unit area.
The sharpness of the switching behaviour of the MOSFET is characterized by the subthreshold swing (SS), also referred to as the inverse subthreshold slope. The SS is defined as the voltage required to increase the drain current by a decade. The expression for SS is given as follows

$$S = \left(\frac{dV_{gs}}{dlog(I_{ds})}\right) = 2.3\left(\frac{KT}{q}\right) \cdot \left(1 + \frac{C_d}{C_{SiO_2}}\right) \tag{3.3}$$

where $C_d = C_{dep} + C_{trap}$ is the sum of depletion and trap capacitance.

The threshold voltage (V_T) is extracted using the transfer curve linear extrapolation method. In this method, the tangent line in the linear regime of the transfer curve (40 V to 70 V) is linearly extrapolated to V_{gs} as shown in figure 3.2 (b). The x-intercept gives the V_T.

Drain-induced barrier lowering (DIBL) is a short channel effect which is referred to as a decrease in threshold voltage with an increase in drain-source voltage. The DIBL is defined as the ratio of the lateral shift of the transfer curves in the subthreshold

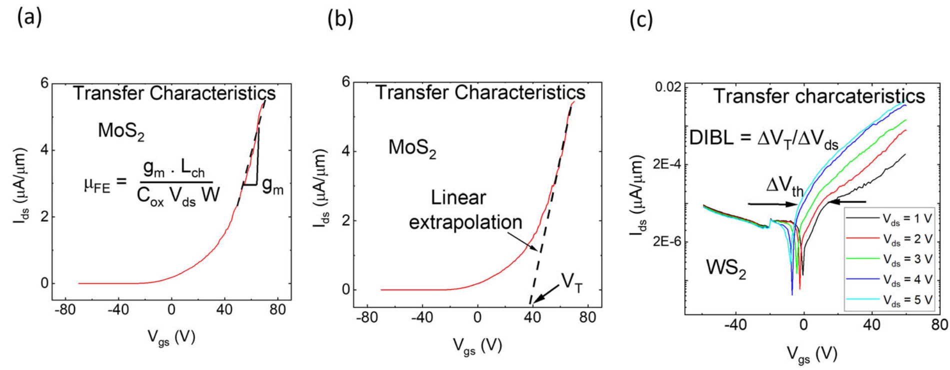

Figure 3.2: (a) Field effect mobility of MoS_2 extracted using the transconductance of the linear regime. (b) Transfer characteristics showing the extracted threshold voltage using linear extrapolation method (c) The transfer characteristics of WS_2 for different V_{ds} in logarithmic scale showing the presence of drain-induced barrier lowering phenomenon.

regime (Δ V_T) and the drain voltage difference of the two curves. The unit of DIBL is V/V. Figure 3.2 (c) shows the observed DIBL in WS_2.

4

Results and Discussion

2D TMDs are promising candidates for atomically thin transistors. 2D TMDs and heterostructures are also being explored for ultrathin photodetectors because of their strong light-matter interaction and broadband photoresponse. In this thesis, electrical and optoelectronic characterization of MoS_2-WS_2 lateral heterostructure are done. Schottky barrier height (SBH) of MoS_2 and WS_2 are extracted by fitting the I-V curves with the back-to-back-diode model. Photoresponsivity and gain factors are measured. Persistent photoconductivity (PPC) effect is also observed at the heterojunction. In the literature, the demonstration of the PPC effect is only limited to MoS_2 and WS_2. Here, we demonstrated the PPC effect at the heterojunction.

4.1 Experimental Details

MoS_2-WS_2 lateral heterostructures grown using the water-assisted one-pot CVD method are used to design the FETs. First, the LHS are transferred to the target substrate (Si/SiO_2) using the PMMA wet transfer technique [45]. SiO_2 of thickness 250 nm is used as a back gate. Next, suitable flakes are identified using an optical microscope and rectangular channels of length 5 microns are patterned using e-beam lithography and CHF_3/Ar etching. Ti (20nm) /Au (80 nm) contacts are deposited on MoS_2 and WS_2 using an electron beam evaporator. The double-layer resist method is used to improve the resolution. After the device fabrication, the electrical characterization is done using a semiconductor parameter analyzer in a probe station. All measurements are done at room temperature and in vacuum conditions. The optoelectronic characterization is performed by illuminating the sample with green laser light of 1.3W with a beam size of 25 μm^2.

4.2 Electrical Characterization

Figure 4.1(a) shows the optical image of the fabricated MoS_2-WS_2 lateral heterostructure FET device and a schematic diagram of the device. The dotted black line represents the MoS_2-WS_2 heterojunctions. The measured output characteristics of MoS_2 and WS_2 are shown in Figure 4.1(b) and 4.1(c) respectively. The exponential increase of drain current at low bias shows the presence of Schottky barrier contacts [1]. Figure 4.1(d) and 4.1(e) shows the transfer characteristics. Both MoS_2 and WS_2 shows n-type characteristics behaviour with threshold voltage (V_T) of about 25 V and 33 V respectively. Since the WS_2 has higher V_T than MoS_2

there exists a $n^+ - n$ junction at the heterojunction, where MoS_2 is n^+ doped while WS_2 is n doped.

The field effect mobility is calculated using the following expression

$$\mu = \left(\frac{dI_{ds}}{dV_{gs}}\right) \cdot \left(\frac{L_{ch}}{W_{ch}.C_{ox}.V_D}\right) \tag{4.1}$$

where L_{ch}, W_{ch} and C_{ox} are the channel length, channel width and capacitance per unit area. The channel width is 5 μm. The capacitance of SiO_2 is found to be 0.012 $\mu F/cm^2$. The calculated μ is about 0.06 $cm^2V^{-1}s^{-1}$ in L_{ch} = 4 μm for MoS_2 and 0.001 $cm^2V^{-1}s^{-1}$ in L_{ch} = 0.52 μm for WS_2 . The very low field effect mobility is due to the presence of large Schottky barrier height [29] and structural defects [46] which act as electron scattering centres. Structural defects such as grain boundaries, vacancies, and substitutional doping are unintentionally generated due to the fluctuating growth conditions during the CVD method [28]. Ripples, folding, and wrinkles are also common 2D structural defects observed during the growth and transfer process [26]. The thermal expansion coefficient mismatch between TMD and substrate results in the formation of ripples during the CVD growth. The subthreshold slope (SS) is calculated using the following expression,

$$S = \left(\frac{dV_{gs}}{dlog(I_{ds})}\right) = 2.3\left(\frac{KT}{q}\right) \cdot \left(1 + \frac{C_d}{C_{SiO_2}}\right) \tag{4.2}$$

where $C_d = C_{dep} + C_{trap}$ is the sum of depletion and trap capacitance [47]. The minimum SS is found to be around 2 V/dec for both MoS_2 and WS_2. The observed large value of SS is because of the thick SiO_2 which increases the interface trap density [48]. High interface trap density increases the depletion capacitance which results in a large SS. The best performing MoS_2 device showed I_{max}/I_{min} ratio in the order of 10^3 with I_{max} of 1.1 × 10^{-2} $\mu A/\mu m$ and I_{min} of 1.7 × 10^{-7} $\mu A/\mu m$, and a DIBL of 6 V/V. WS_2 showed I_{max}/I_{min} ratio of 3 × 10^2 with I_{max} of 7.4 × 10-3 $\mu A/\mu m$ and I_{min} of 3 × 10^{-7} $\mu A/\mu m$, and a DIBL of 3 V/V.

All the measurements discussed so far are for pristine material. To improve the electrical performance of MoS_2-WS_2 lateral heterostructure, we annealed the sample at 180^oC for 2 hrs in Ar/H_2 environment. Annealing the sample has increased the mobility from 0.04 $cm^2V^{-1}s^{-1}$ to 0.45 $cm^2V^{-1}s^{-1}$, decreased the V_T by ΔV_T = -10 V, enhanced the I_{max}/I_{min} by 10^2 orders, and significantly decreased the SS and DIBL by 1.3 V/dec and 3 V/V respectively. The transfer characteristic comparison of annealed and pristine MoS_2 is shown in figure 4.1 (f). The enhancement of the device electrical properties after annealing is due to the improved crystal quality, elimination of defects and impurities such as organic photoresists residues, enhanced carrier mobilities, and reduced Schottky barrier height (SBH) by reducing the metal work function [49]. Annealing enhances the electrical conductivity by influencing the crystal domains and crystal grain boundaries. Moreover, annealing of TMDs

reduces the tunnelling barrier and van der Waals gap between the TMD and metals by forming an alloyed metal- TMD interface [50]. In addition, annealing can also influence the optical properties of TMDs by modifying the bandgap energy [51]. Generally, the effects of annealing depend on the annealing temperature, duration, and environment.

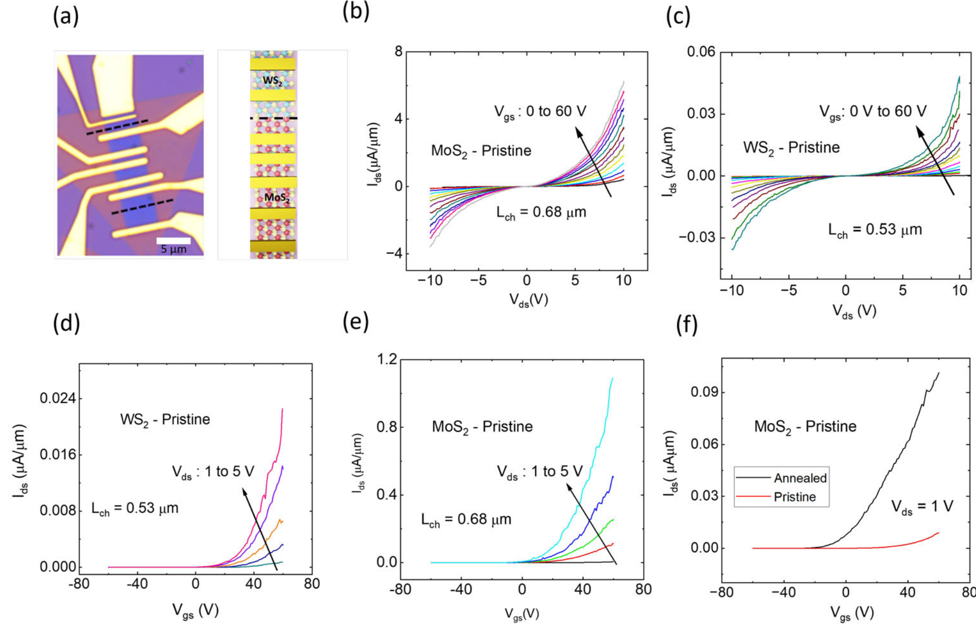

Figure 4.1: Electrical characterization of MoS_2 and WS_2 (a) Optical image of the fabricated MoS_2 - WS_2 LHS FET. The dotted black line represents the heterojunctions. Ti/Au is used as a contact metal. The interior and exterior region corresponds to the MoS_2 and WS_2 respectively. (b), (c) Output characteristics of MoS_2 and WS_2 at different gate voltages (V_{gs}) respectively. V_{gs} increases in a step of 5 V. The exponential increase of current shows the presence of Schottky barrier contact. (d), (e) Transfer characteristics of MoS_2 and WS_2 at different drain-source voltages (V_{gs}) respectively. (f) Transfer characteristics curve of a pristine MoS_2 and annealed MoS_2 at V_{ds} =1 V. The sample is annealed in Ar/H_2 at 180^oC for 2 hrs.

Figure 4.2 (a) shows the schematic diagram of the MoS_2-WS_2 heterojunction. Figure 4.2 (b) shows the output characteristic curves of the heterojunction for different gate voltages. A low drain current during the reverse bias and an exponential increase of drain current in the forward bias confirms the rectifying behaviour of the heterojunction. The rectifying behaviour arises because of the internal band bending which occurs due to the difference in the fermi level of MoS_2 and WS_2. Figure 4.2 (b) shows the transfer characteristic curve for different drain-source voltages. The heterojunction showed n-type characteristic behaviour. Figure 4.2 (d) shows the formation of internal band bending at the heterojunction using the energy band diagram. The fermi level of MoS_2 lies closer towards the conduction band edge than WS_2. The best perforing heterojunction showed a mobility of 0.13 $cm^2V^{-1}s^{-1}$, I_{max}/I_{min} ratio of 3 × 10^3 and SS of 4.4 V/dec. The ON-OFF ratio of the heterojunction is around 10^2 which is low when compared to p-n junctions based on 2D

TMDs [52] [53]. Figure 4.2 (e) and 4.2 (f) compares the output and transfer curves of pristine and annealed heterojunction. Annealing has increased the mobility to $0.47cm^2V^{-1}s^{-1}$, decreased the SS to 2.4 V/dec and increased the I_{max}/I_{min} ratio to 2×10^4.

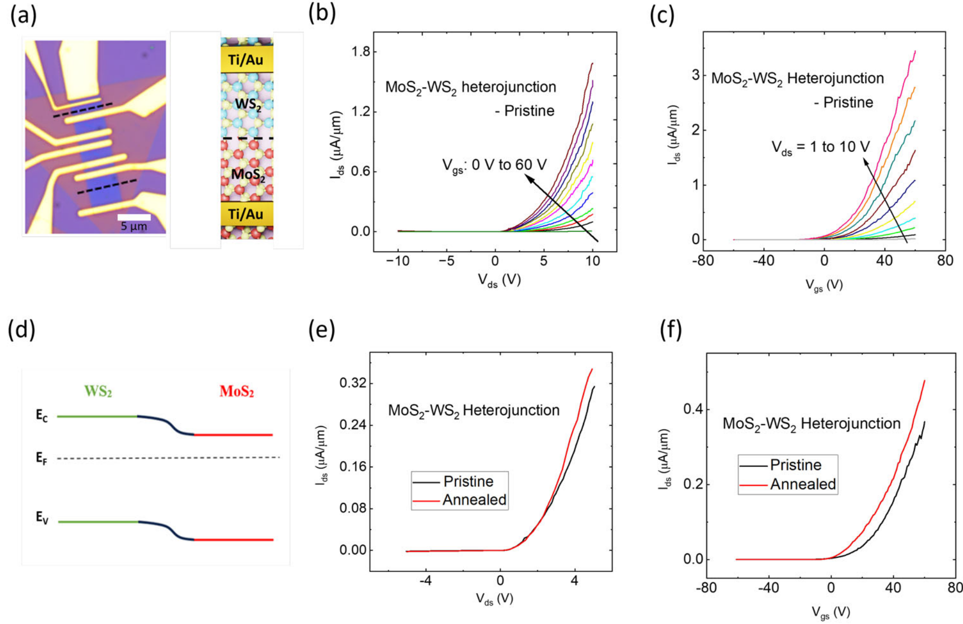

Figure 4.2: Electrical characterization of MoS_2-WS_2 lateral heterojunctions(a) Optical image of the fabricated MoS_2-WS_2 LHS FET. (b) Output characteristics of the heterojunction showing rectifying behaviour. Since the heterojunction is $n - n^+$ doped, a low on-off ratio is observed. (c) Transfer characteristics of the heterojunction for different drain voltages. (d) Energy band diagram at the heterojunction. The difference in the carrier concentration between MoS_2 and WS_2 causes the formation of internal band bending. (e), (f) Output and transfer characteristics curve comparison of pristine and annealed heterojunctions.

Figure 4.3 shows the temperature dependent measurements for MoS_2 and WS_2. We varied the temperature from 100K to 300K in the step of 50 K and extracted the field effect mobility from the transfer characteristic curves. We observed that the mobility increases with the temperature at V_{ds} = 1 V. The observed increase in mobility with the temperature as shown in figure 4.3 (c) confirms the presence of a thermionic electron emission current injection mechanism at the metal-TMD Schottky contact interface [54]. In an ideal Schottky contact, the current density equation is given as follows,

$$J_1 = J_o(e^{qV_1/KT} - 1) \tag{4.3}$$

where J_o is the reverse saturation current density which originates from the thermionic emission mechanism. The relationship between J_o and temperature is given by the Richardson formula:

$$log\left(\frac{J_o}{T^{\beta}}\right) = A - \frac{B}{T} \tag{4.4}$$

where β is the scaling exponent term which depends on the type of Schottky contact formed at the metal-TMD interfaces, A and B are material/interface dependent constants. Generally, there are two types of Schottky contacts found in 2D materials: vertical Schottky contacts and lateral Schottky contacts[55].

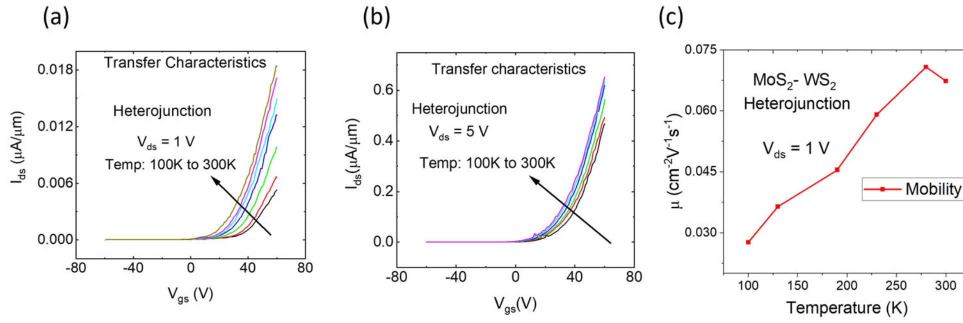

Figure 4.3: Temperature dependent data:(a),(b) Transfer characteristics at V_{ds}=1 V and V_{ds}=5 V for temperature ranging from 100 K to 300 K respectively. (c) Dependence of field effect mobility on temperature for V_{ds}=1 V.

4.3 Schottky barrier height extraction

The Schottky barriers are often formed at the metal/TMD interface and have a strong influence on the electrical behaviour of the monolayer and bilayer TMDs. Therefore, for a better understanding of the device physics, it is essential to extract the SBH accurately. We extracted the SBHs at Ti/Au contacted MoS_2, WS_2, using two methods: (a) Double Schottky barrier model and (b) Richardson's equation. The Richardson's constants of MoS_2 and WS_2 are calculated using their corresponding electron effective masses. MoS_2 and WS_2 has an effective mass of 0.4*m_e and 0.34*m_e respectively [56]. The obtained value of Richrdson's constant for MoS_2 and WS_2 are 47 $Acm^{-2}K^{-1}$ and 40.47 $Acm^{-2}K^{-1}$ respectively.

Although the Arrhenius method is widely used for the SBH extraction in 2D TMDs, the presence of surface defects and van-der-Waals gap results in a weak temperature-dependent thermionic current which often leads to erroneous SBH [57]. At temperatures below 100 K, the thermionic current is significantly suppressed in contact-dominated 2D TMD FETs with considerable SBH >100 eV. This makes it extremely difficult to measure the current at lower temperatures.

In 2D TMDs, since the SBH is strongly influenced by the interfacial chemistry and structural defects, there is a possibility that SBH might be different at drain and source metal electrodes. Therefore, it is prudent to extract both the SBHs. Figure 4.4(a) shows the energy band diagram with two different SBH at the source and drain contacts. We have used the back-to-back diode model which allows the extraction of SBH at both the contacts (drain and source electrodes) [58], [59]. In this model, the thermionic current at each contact is given by

$$I_1 = I_{s1}(e^{qV_1/KT} - 1) \tag{4.5}$$

$$I_2 = -I_{s2}(e^{qV_2/KT} - 1) \tag{4.6}$$

where

$$I_{s1,s2} = S_{1,2}A^*T^2e^{-(\phi_{B01,B02}/KT)} \tag{4.7}$$

are the reverse saturation current, $V_{1,2}$ are the voltage drop across the contacts which are assumed to be V/2, $S_{1,2}$ are the contact areas, A^* is the Richardson constant, T is the temperature, ϕ_{B01} and ϕ_{B02} are the Schottky barriers heights. The total current through the device, the sum of I_{s1} and I_{s1} is expressed as

$$I_{tot} = \frac{2I_{s1}I_{s2}sinh\left(\frac{qV}{2KT}\right)}{I_{s1}e^{\frac{qV}{2KT}} + I_{s2}e^{\frac{-qV}{2KT}}} \tag{4.8}$$

To include the effects of the interface oxides and structural defects, the Schottky barriers are replaced with an effective Schottky barrier that includes the effects of image charge lowering and ideality factors. The effective barriers are expressed as

$$\phi_{B1,B2} = \phi_{B01,B02} \pm eV_{1,2}\left(1 - \frac{1}{n_{1,2}}\right) \tag{4.9}$$

where $n_{1,2}$ is the ideality factor at the contacts.

Figure 4.4(b) and 4.4(c) shows the model fitting of output characteristics curve for MoS_2-WS_2 at V_{gs} = 60 V. The extracted SBH are ϕ_1 = 0.45 eV, and ϕ_2 =0.42 eV for MoS_2 and ϕ_{B1} = 0.5 eV, ϕ_{B2} = 0.48 eV for WS_2. The most significant difference between the model and the data is the low bias nonlinearity, which is highlighted by the black circle. This prominent deviation at low bias is due to the absence of inclusion of series resistance in the model [60]. We found that there was no significant difference between the SBHs at the source and drain contacts and the ideality constants were nearly unity.

Unlike the Arrhenius method which requires the analysis of temperature-dependent transfer and output characteristics curves, the Richardson method requires the analysis of output curves at constant temperature [61]. The Richardson's equation is rearranged as

$$ln\left[\frac{I_{ds}exp(qV_{ds}/K_BT)}{exp(qV_{ds}/K_BT) - 1}\right] = ln(I_o) + (qV_{ds}/KT) \tag{4.10}$$

The Schottky barrier and ideality constant are determined from the y-intercept and slope of the above equation in the negative V_{ds} regime.

In SB contacts, the current injection takes place through two mechanisms: (a) Thermionic emission current ($I_{thermionic}$) and (b) tunnelling/field emission current (I_{tunnel}). Figure 4.4(d) illustrates the current injection mechanism at the metal-semiconductor interface. In $I_{thermionic}$, the charge carriers pass over the top of SB. Whereas in I_{tunnel}, the charge carriers pass through the SB when there is a sufficiently small SB width. The dominance of these two components is controlled by V_{gs}, At low V_{gs}, I_{tunnel} component is negligible because of the large SB width, and therefore only $I_{thermionic}$ dominates. But at high V_{gs}, the smaller SB width increases the probability of tunnelling current, thus making the I_{tunnel} component dominate. The actual SBH is calculated from the $\phi_{B,eff}$ vs V_{gs} plot by identifying the $\phi_{B,eff}$ at the flat band voltage (V_{FB}). The V_{FB} is the voltage at which the energy band at the metal-semiconductor interface appears flat because of the zero surface potential. Due to the exponential dependence of $\phi_{B,eff}$ on V_{gs} for $V_{gs} < V_{FB}$, a linear dependence is observed in the Arrhenius curve. When $V_{gs} < V_{FB}$, the thermionic current dominates. However, at $V_{gs} > V_{FB}$ the $\phi_{B,eff}$ shows a weak dependence on V_{gs}, because of the dominance of tunnelling current, which results in the deviation of initial linearity. At V_{FB}, the $\phi_{B,eff}$ tends to deviate away from the initial linear dependency due to the thermionic- tunnelling regime transition.

Figure 4.4(e) compares the SBHs extracted from the back-to-back diode model and Richardson's model. We observed not much disagreement between these two models. The effective SBH of MoS_2 was around 0.35 eV, which is comparable with

previous works [58], [62]. The effective SBH of WS_2 couldn't be extracted, since there wasn't any clear transition between tunnelling and thermionic regime. Figure 4.4(f) compares the SBH of MoS_2 and WS_2. WS_2 has higher SBH than MoS_2, which explains the poor performance of WS_2. The large SB height obtained for MoS_2 and WS_2 which prevents efficient injection of carriers from the contact metal into the channel is responsible for high contact resistance [63]. This unexpectedly large SBH arises due to fermi-level pinning (FLP). FLP has been often observed in 2D TMDs and they are caused by the presence of extrinsic contributors such as metal-induced gap states (MIGS), interface dipoles, and intrinsic contributors such as structural defects and defect-induced gap states (DIGS) [64].

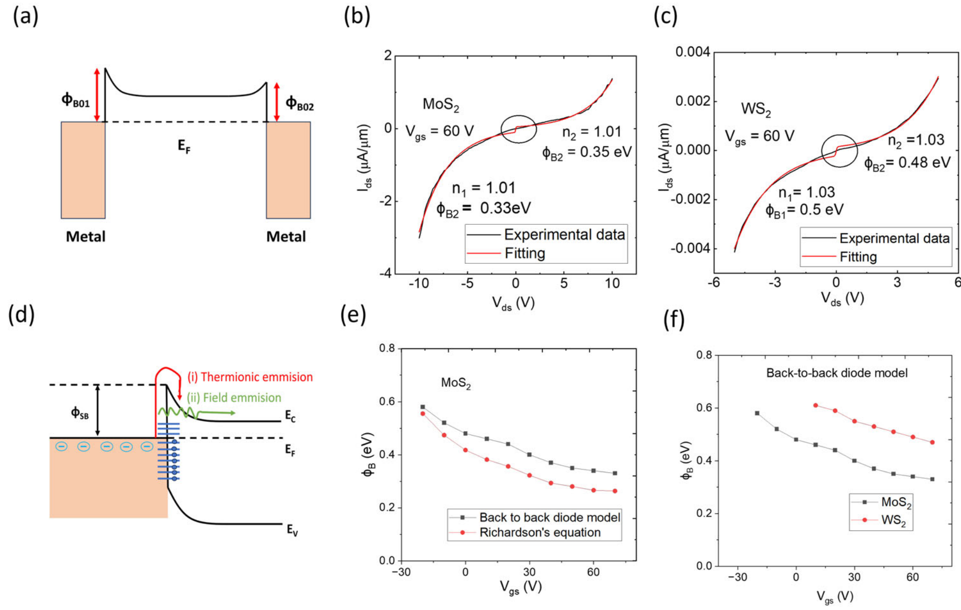

Figure 4.4: Extraction of Schottky barrier height (SBH): (a) Energy diagram of 2D TMDs showing two different SBH at the metal contacts for an unbiased condition (V_{ds}=0). The strong dependence of SBH on structural defects at the metal-TMD interface might result in different SBH at source and drain contacts. (b-c) Output characteristic curve of MoS_2 and WS_2, for V_{gs} = 60 V. The experimental data (black line) were fitted with a back-to-back diode model (red line) with SBH and ideality factor as fitting parameters. (d) Schematic diagram explaining the current injection mechanism at the Schottky barrier contact. (e) Comparison between back-to-back diode model and Richardson model. (f) Comparison of net SBH between MoS_2 and WS_2.

4.4 Optoelectronic characterization

To study the optoelectronic properties, we used a green laser light of 1.65 W to illuminate the sample and measured the output and transfer characteristics. The beam size of the laser is around 25 μm^2. Figure 4.5(a) shows the schematic of the sample with the experimental setup. Figure 4.5(b) and 4.5(c) shows the measured transfer characteristics curves and photocurrent under green laser light at the heterojunction respectively. The photocurrent is calculated by subtracting the dark current from the current under laser illumination (Eq 4.11).

$$I_{photo} = I_{light} - I_{dark} \tag{4.11}$$

The illumination had drastically decreased the threshold voltage by 10 V, increased the I_{max}/I_{min} by 10 times, slightly increased the carrier mobility from 0.47 $cm^2V^{-1}s^{-1}$ to 0.62 $cm^2V^{-1}s^{-1}$. We also observed an increase in hysteresis.

Generally, there are two mechanisms through which photocurrents are generated: (i) photoconductive effect and (ii) photogating effect [65]. In the photoconductive effect, the photoexcited electron-hole pairs increase the free carrier concentration in the conduction and valence band, and these carriers drift towards their respective metal electrodes by the external bias (V_{ds}), thus generating the photocurrent. The photogating effect occurs due to the traps present near the band edges, which become charged upon illumination and give a gating effect to the device [66]. The shift in threshold voltage upon optical excitation is a tell-tale sign of the photogating effect. In our sample, the MoS_2, WS_2 and heterojunction showed a significant negative threshold voltage shift (ΔV_T) of -17 V, -26 V, and -11 V respectively, upon laser excitation. Since the sign of ΔV_T is opposite of the polarity of the trapped charges, the negative shift shows that the traps at the proximity of the valence band edge become positive charges upon illumination and these positive charges shift the fermi level towards the conduction band thus increases the electron concentration. The increase in hysteresis further confirms the presence of traps [67]. Figures 4.5 (d) and 4.5 (e) schematically explain the photoconductive and photogating effects respectively.

We conclude that our sample is dominated by the photogating effect because of the observed strong dependence of photocurrent on V_{gs}. The photoconductive effect is less dependent on V_{gs} [68], [42] whereas the photogating effect is strongly dependent on V_{gs}.

To measure the sensitivity of the lateral heterojunction to the incident laser light, we calculated the photoresponsivity. The photoresponsivity is defined as a ratio between photocurrent and total optical power (Eq 4.12).

$$R = I_{Ph}/P_A \tag{4.12}$$

where R is the photoresponsivity, I_{ph} is the measured photocurrent, and P_A is the total incident power imping on the detection area. The calculated photoresponsivity of the heterojunction is around 0.2 A/W at V_{ds} =1 V and V_{gs} = 0 V. The photoresponsivity increases with source-drain voltages. It reaches 2.6 A/W at V_{ds} = 5 V. We also calculated the gain factor, which is defined as the number of charge carriers flowing through the circuit per photogenerated electron-hole pair [69].

$$G = (h\nu)/(e\eta)R \tag{4.13}$$

where R is the photo responsivity, h is plank constant, ν is the frequency of laser light, η is the light absorption rate and e is the absolute value of electron charge. By assuming a light absorption rate of 8 % [70], the calculated gain factor of heterojunction is found to be 6 for R = 0.2 A/W. We also observed an exponential dependence of the gain factor with source-drain bias.

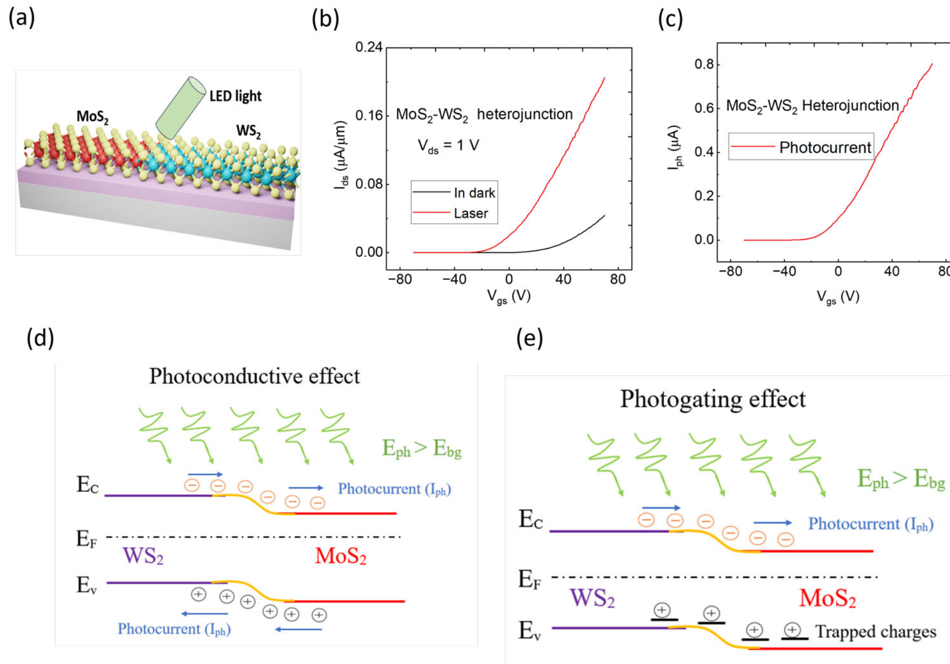

Figure 4.5: Optoelectronic characteristics of a MoS_2-WS_2 heterojunction(a) Schematic drawing of the MoS_2- WS_2 heterojunction FET with the experimental setup. (b) Comparison of transfer characteristics under green LED laser with dark condition. (c) Plot showing the extracted photocurrent (I_{ph}) at the heterojunction. The photocurrent is obtained by subtracting the dark current from the current under laser illumination. The photocurrent increases with the gate voltage. (d) Possible photoconductivity mechanism in MoS_2-WS_2 heterostructure: Photoconductive and photogating effect.

Schottky barrier height dependence on gate voltage in dark conditions and under laser light for MoS_2 and WS_2 are shown in Figure 4.6(a) and 4.6(b). It's observed that, upon laser illumination, the SBH decreased appreciably. For MoS_2, the SBH decreases from 0.5 eV to 0.3 eV at $V_{gs} = 0$ V. This lowering of the net SBH is due to the presence of trapped charges at the metal-TMD interfaces [71]. The observed hysteresis confirms the presence of mid-gap trap states. The applied external bias makes the photogenerated electrons and holes drift toward their respective electrodes. Although photogenerated electrons easily reach the positive electrode (anode), the photogenerated holes get trapped at the metal-TMD interface near the negative electrode (cathode). This formation of positively charged trap states increases the electron carrier concentration in the TMDs, thus moving the fermi level toward the conduction band at the metal-TMD interface. This leads to a significant reduction of SBH. Figure 4.6(c) schematically explains the photoinduced SBH lowering. Similar photoinduced trapped holes accumulation at the metal-semiconductor interface is reported for Au-WS_2 [72] and GaAs MSM photodetectors [73] [74] [75].

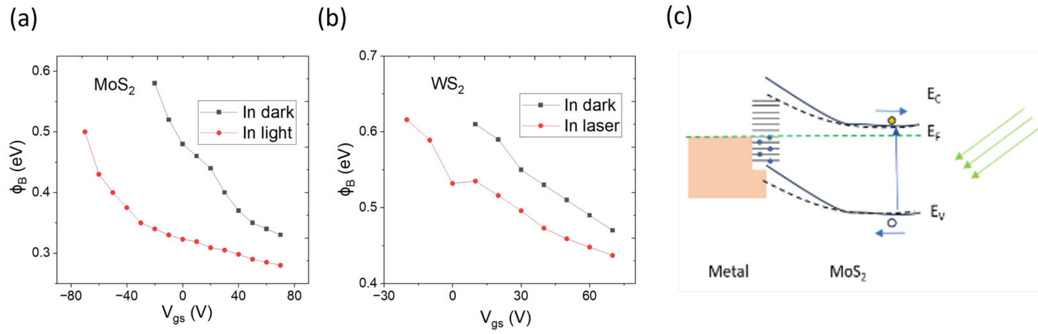

Figure 4.6: Photoinduced Schottky barrier lowering (a), (b) Dependence of net SBH on gate voltage for MoS_2 and WS_2 respectively. Noticeable SBH lowering upon laser illumination is observed. The SBH is extracted using a double Schottky barrier model. (c) Band diagram of metal-MoS_2 illustrating the photoinduced Schottky barrier height lowering. The mid-gap trap states, which influence the SBH through the fermi level pinning effect are shown. Upon illumination, electron-hole pairs are generated. The photogenerated holes drift towards the cathode (negative electrode) and get trapped at the metal-semiconductor interface, thus lowering the effective SBH. The dashed and solid line denotes the energy band position before and after illumination respectively.

4.5 Persistent Photoconductivity

We also measured the photoconductivity after the termination of laser light. Measuring the photoconductivity after the termination of light in photodetectors can help us understand the response time and speed. The decay characteristics of photoconductivity can also reveal the presence of trap states and defects in the channel materials. In MoS_2, WS_2 and heterojunction, the photoconductivity persists for several hours. The decay of the drain current is fitted with a double decay exponential curve,

$$I = I_o + A_1 exp(-t/\tau_1) + A_2 exp(-t/\tau_2) \tag{4.14}$$

where τ_1 and τ_2 are the two characteristics time constants. We observed that τ_1 (order of 10^2 sec) was much smaller than τ_2 (order of 10^3 sec), which explains the observed rapid decay of photoconductivity immediately after the turn-off of the laser illumination. The exp (-t/ τ_1) term corresponds to the regime immediately after the termination of laser light and exp (-t/ τ_2) corresponds to the regime long after the termination of laser light. Figure 4.7(a), 4.7(b) and 4.7(c) shows the observed PPC for MoS_2, WS_2 and heterojunction measured at V_{ds}= 1 V and V_{gs} = 70V. The extracted time constants at the MoS_2-WS_2 heterojunction were τ_1 = 2,600 sec and τ_2 =37,000 sec. Similar values were obtained for MoS_2 (τ_1= 1,660 sec and τ_2 =37,000 sec). However, WS_2 showed a faster decay process with τ_1= 915 sec and τ_2 =1,400 sec.

During the measurement, the laser light was turned off once the photocurrent saturates. Since the time taken by the photocurrent to become sufficiently saturate is not the same for all the measurement cases, we couldn't maintain a constant laser illumination time. This is because the materials didn't recover fully from the previous laser illumination, and the initial state of the current was not same.

This double exponential decay phenomenon was also observed in several semiconductor materials such as CdS, ZnO, and WO_3 [76] [77]. The variable decay rates in CdS FETs are caused by the non-uniform thickness of CdS [78]. In metal oxides such as ZnO, the type of oxygen adsorption mechanism (i.e physisorption and chemisorption of oxygen) leads to variable trapping rates and results in different decay processes [79].

The observed double decay process in our study could be attributed to the band-to-band transition, and the charge trapping at the extrinsic and intrinsic defects. Generally, the band-to-band transition (i,e electron-hole recombination) is a dominant mechanism for the initial rapid decay rate process. The presence of shallower traps can also be attributed to the shorter decay component. The observed PPC after the initial drop can be explained through the random local potential fluctuations (RLPF) model. According to this model, the local fluctuations of the potential energy of carriers arise due to extrinsic charge impurities and intrinsic structural effects [37]. Upon laser illumination, the photoexcited carriers get trapped at the

local potential minima/deep traps and cause a decrease in the rate of recombination, which leads to PPC. Figure 4.7 (d) illustrates the spatial potential fluctuations at the conduction and valence band edge proximity.

Extrinsic defects such as alloy disorder, photoresist contaminants during the lithography process, and substrate effects are predominant in 2D TMDs. Previous study [14] on the substrate effects of PPC on MoS_2 confirmed that PPC arises due to charge trapping by the gas adsorbates/chemical impurities [80], [81] present at the TMD-SiO_2 interface, by comparing the PPC effects with a substrate supported and suspended MoS_2 devices. Intrinsic structural defects such as chalcogen vacancies, and substitutional doping are often observed in TMDs. Ripples, wrinkles, and folding are also common 2D structural defects observed which contribute to the potential fluctuations. These 2D structural defects are observed during the growth and transfer process. After the TMDs are grown at high temperatures, during cooling the thermal expansion coefficient mismatch between TMD and substrate results in the formation of biaxial strain [82]. This local lattice strain results in an inhomogeneous charge distribution, and surface potential and shifts the energy level of materials near the fermi level which leads to the fluctuations in band structure[83]. Therefore, analyzing the decay characteristics of persistent photoconductivity can help us understand the effect of structural defects and substrate interface on the photoresponse of the photodetectors.

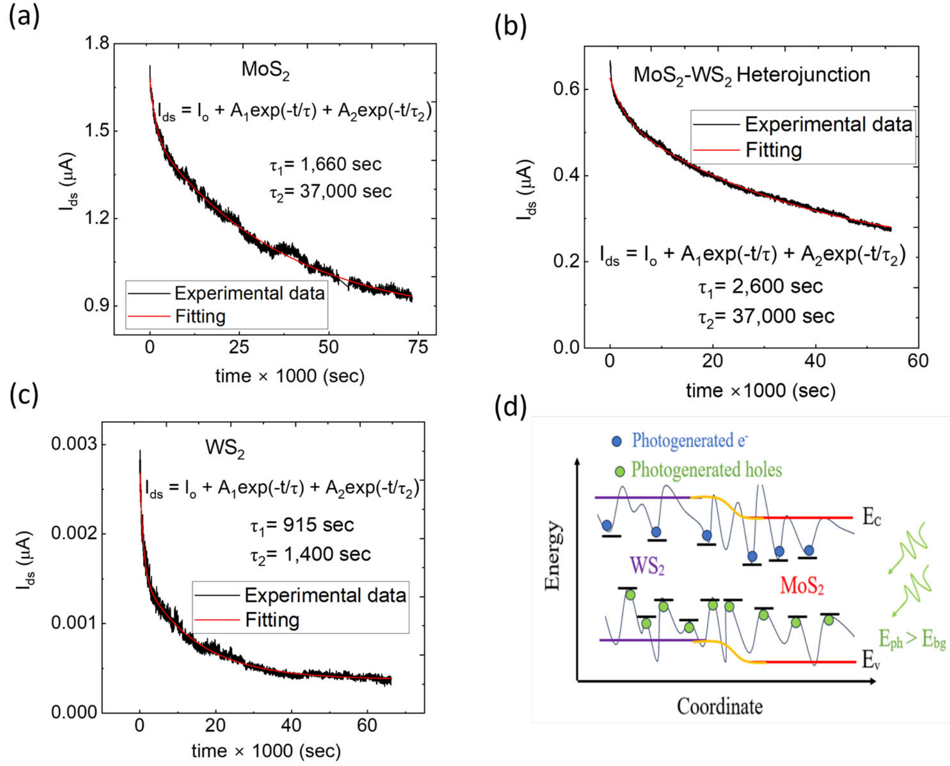

Figure 4.7: Experimental observation of persistent photoconductivity (PPC). (a), (b), (c) Decay of drain current with time after the termination of laser light for MoS_2, WS_2, and MoS_2-WS_2 heterojunction measured at V_{ds} = 1V and V_{gs} = 70 V under vacuum. The sample is illuminated at V_{gs} = 70 V. The drain current decay is fitted with a double decay exponential curve to extract the carrier recombination lifetime. (d) Illustration of spatial fluctuations of potential energy near the conduction and valence band edges. The photoexcited electrons and holes gets trapped at the local potential minima and take a longer time to recombine which results in a persistent photoconductivity. The potential fluctuations are caused by extrinsic defects (substrate effects, surface adsorbates, photoresist contaminants during the lithographic process), and intrinsic defects such as chalcogen vacancies, grain boundaries, ripples, etc. The illustration is adapted from [15].

5

Summary and Conclusions

Atomically thin, dangling bond-free 2D TMDs are promising channel materials for next-generation transistors because of their ability to retain their carrier mobilities down to monolayer thickness. TMDs such as MoS_2, $MoSe_2$, WS_2, and WSe_2 are being widely researched. 2D TMDs are also promising candidates for ultrathin photodetectors due to their strong light-matter interaction and broadband photoresponses. TMD lateral heterostructures offer several advantages over single TMDs for optoelectronic applications. Photodetectors with ultrahigh photoresponsivity have been reported recently. Persistent Photoconductivity (PPC) effect has been observed in 2D TMDs. The PPC effect is being explored for optoelectronic synapses, optical memory and artificial vision applications. The demonstration of the PPC effect is only limited to single TMDs such as MoS_2, $MoSe_2$, WS_2, and WSe_2.

In this master's thesis, MoS_2-WS_2 lateral heterostructure field effect transistor is fabricated and electrical and optoelectronic characterization are performed. MoS_2-WS_2 lateral heterostructures grown using the water-assisted one-pot CVD method are used for the FET fabrication. We used the PMMA wet transfer technique to transfer the as-grown lateral heterostructures to the target substrate (SiO_2/Si). Ti(20nm)/Au(80nm) metal contacts are deposited on MoS_2 and WS_2. A green laser light of 1.3W is used to illuminate the sample for the optoelectronic characterization. The electrical measurements are done at room temperature and vacuum conditions.

Both MoS_2 and WS_2 showed n-type characteristics behaviour. We observed a Schottky barrier contact between the metal/TMD interface. We observed a very low field-effect mobility due to the presence of 2D structural defects such as grain boundaries, wrinkles, and folding which arises during the growth and transfer process. Since the WS_2 has a higher threshold voltage than MoS_2, a n^+-n junction is formed at the MoS_2-WS_2 heterojunction, where MoS_2 is n^+ doped and WS_2 is n doped. A rectifying behaviour is observed at the heterojunction due to the internal band bending.

The Schottky barrier height (SBH) of MoS_2 and WS_2 is extracted using a back-to-back diode model and Richardson's model. The effective SBH of Mos_2 is around 0.35 eV which is comparable with the previous works. The large SBH arises due to high contact resistances. The contact resistance extracted using transfer length analysis is found to be in the range of a few M$\Omega.\mu$m.

We get a potoresponsivity of 0.2 A/W at V_{ds}= 1 V and a gain factor of 6 for R = 0.2 A/W at the MoS_2-WS_2 heterojunction. A significant decrease in the threshold voltage and an increase in hysteresis is observed upon illumination of green laser

light. We conclude that the photoconductive effect at heterojunction is dominated by the photogating effect. We also noted that the SBH decreased appreciably upon illumination.

The persistent photoconductivity (PPC) effect is also demonstrated at the MoS_2-WS_2 heterojunction. A time constant of around 10 hours is observed. The PPC effect arises due to random potential fluctuations caused by the extrinsic charge impurities and intrinsic structural defects.

In summary, the electrical and optoelectronic characterization of MoS_2-WS_2 heterostructure FET is successfully performed. The electrical and optical properties of the lateral heterostructure FETs are strongly dependent on structural defects, charge impurities, and large contact resistances. These findings are important as they contribute to an understanding of the physics of 2D TMD lateral heterostructure devices for future applications.

Bibliography

[1] J. A. del Alamo, *Integrated microelectronic devices : physics and modeling, Chapter:10*. NY, NY : Pearson, [2018], first ed.

[2] S. Takagi, A. Toriumi, M. Iwase, and H. Tango, "On the universality of inversion layer mobility in Si MOSFET's: Part I-effects of substrate impurity concentration," *IEEE Transactions on Electron Devices*, vol. 41, pp. 2357–2362, Dec. 1994.

[3] J. Robertson, "High dielectric constant gate oxides for metal oxide Si transistors," *Reports on Progress in Physics*, vol. 69, p. 327, Dec. 2005.

[4] S. Thompson, M. Armstrong, C. Auth, S. Cea, R. Chau, G. Glass, T. Hoffman, J. Klaus, Z. Ma, B. Mcintyre, A. Murthy, B. Obradovic, L. Shifren, S. Sivakumar, S. Tyagi, T. Ghani, K. Mistry, M. Bohr, and Y. El-Mansy, "A logic nanotechnology featuring strained-silicon," *IEEE Electron Device Letters*, vol. 25, pp. 191–193, Apr. 2004.

[5] A. Razavieh, P. Zeitzoff, and E. J. Nowak, "Challenges and Limitations of CMOS Scaling for FinFET and Beyond Architectures," *IEEE Transactions on Nanotechnology*, vol. 18, pp. 999–1004, 2019.

[6] N. Loubet, T. Hook, P. Montanini, C.-W. Yeung, S. Kanakasabapathy, M. Guillom, T. Yamashita, J. Zhang, X. Miao, J. Wang, A. Young, R. Chao, M. Kang, Z. Liu, S. Fan, B. Hamieh, S. Sieg, Y. Mignot, W. Xu, S.-C. Seo, J. Yoo, S. Mochizuki, M. Sankarapandian, O. Kwon, A. Carr, A. Greene, Y. Park, J. Frougier, R. Galatage, R. Bao, J. Shearer, R. Conti, H. Song, D. Lee, D. Kong, Y. Xu, A. Arceo, Z. Bi, P. Xu, R. Muthinti, J. Li, R. Wong, D. Brown, P. Oldiges, R. Robison, J. Arnold, N. Felix, S. Skordas, J. Gaudiello, T. Standaert, H. Jagannathan, D. Corliss, M.-H. Na, A. Knorr, T. Wu, D. Gupta, S. Lian, R. Divakaruni, T. Gow, C. Labelle, S. Lee, V. Paruchuri, H. Bu, and M. Khare, "Stacked nanosheet gate-all-around transistor to enable scaling beyond FinFET," in *2017 Symposium on VLSI Technology*, pp. T230–T231, June 2017. ISSN: 2158-9682.

[7] C. D. English, G. Shine, V. E. Dorgan, K. C. Saraswat, and E. Pop, "Improved Contacts to MoS2 Transistors by Ultra-High Vacuum Metal Deposition," *Nano Letters*, vol. 16, pp. 3824–3830, June 2016.

[8] L. Cheng and Y. Liu, "What Limits the Intrinsic Mobility of Electrons and Holes in Two Dimensional Metal Dichalcogenides?," *Journal of the American Chemical Society*, vol. 140, pp. 17895–17900, Dec. 2018.

[9] Y. Lee, S. Fiore, and M. Luisier, "Ab initio mobility of single-layer MoS2 and WS2: comparison to experiments and impact on the device characteristics," in

2019 IEEE International Electron Devices Meeting (IEDM), pp. 24.4.1–24.4.4, Dec. 2019. ISSN: 2156-017X.

[10] F. H. L. Koppens, T. Mueller, P. Avouris, A. C. Ferrari, M. S. Vitiello, and M. Polini, "Photodetectors based on graphene, other two-dimensional materials and hybrid systems," *Nature Nanotechnology*, vol. 9, pp. 780–793, Oct. 2014.

[11] S. Khan, A. Khan, J. Azadmanjiri, P. Kumar Roy, L. Děkanovský, Z. Sofer, and A. Numan, "2D Heterostructures for Highly Efficient Photodetectors: From Advanced Synthesis to Characterizations, Mechanisms, and Device Applications," *Advanced Photonics Research*, vol. 3, no. 8, p. 2100342, 2022.

[12] M. Chhowalla, H. S. Shin, G. Eda, L.-J. Li, K. P. Loh, and H. Zhang, "The chemistry of two-dimensional layered transition metal dichalcogenide nanosheets," *Nature Chemistry*, vol. 5, pp. 263–275, Apr. 2013.

[13] K. Ye, L. Liu, Y. Liu, A. Nie, K. Zhai, J. Xiang, B. Wang, F. Wen, C. Mu, Z. Zhao, Y. Gong, Z. Liu, and Y. Tian, "Lateral Bilayer MoS2–WS2 Heterostructure Photodetectors with High Responsivity and Detectivity," *Advanced Optical Materials*, vol. 7, no. 20, p. 1900815, 2019.

[14] Y.-C. Wu, C.-H. Liu, S.-Y. Chen, F.-Y. Shih, P.-H. Ho, C.-W. Chen, C.-T. Liang, and W.-H. Wang, "Extrinsic Origin of Persistent Photoconductivity in Monolayer MoS2 Field Effect Transistors," *Scientific Reports*, vol. 5, p. 11472, June 2015.

[15] A. George, M. V. Fistul, M. Gruenewald, D. Kaiser, T. Lehnert, R. Mupparapu, C. Neumann, U. Hübner, M. Schaal, N. Masurkar, L. M. R. Arava, I. Staude, U. Kaiser, T. Fritz, and A. Turchanin, "Giant persistent photoconductivity in monolayer MoS2 field-effect transistors," *npj 2D Materials and Applications*, vol. 5, pp. 1–8, Jan. 2021.

[16] A. Dodda, D. Jayachandran, S. Subbulakshmi Radhakrishnan, A. Pannone, Y. Zhang, N. Trainor, J. M. Redwing, and S. Das, "Bioinspired and Low-Power 2D Machine Vision with Adaptive Machine Learning and Forgetting," *ACS Nano*, vol. 16, pp. 20010–20020, Dec. 2022.

[17] S. K. Chakraborty, B. Kundu, B. Nayak, S. P. Dash, and P. K. Sahoo, "Challenges and opportunities in 2D heterostructures for electronic and optoelectronic devices," *iScience*, vol. 25, p. 103942, Mar. 2022.

[18] C. Huang, S. Wu, A. M. Sanchez, J. J. P. Peters, R. Beanland, J. S. Ross, P. Rivera, W. Yao, D. H. Cobden, and X. Xu, "Lateral heterojunctions within monolayer MoSe2-WSe2 semiconductors," *Nature Materials*, vol. 13, pp. 1096–1101, Dec. 2014.

[19] X. Duan, C. Wang, J. C. Shaw, R. Cheng, Y. Chen, H. Li, X. Wu, Y. Tang, Q. Zhang, A. Pan, J. Jiang, R. Yu, Y. Huang, and X. Duan, "Lateral epitaxial growth of two-dimensional layered semiconductor heterojunctions," *Nature Nanotechnology*, vol. 9, pp. 1024–1030, Dec. 2014.

[20] Z. Zhang, P. Chen, X. Duan, K. Zang, J. Luo, and X. Duan, "Robust epitaxial growth of two-dimensional heterostructures, multiheterostructures, and superlattices," *Science (New York, N.Y.)*, vol. 357, pp. 788–792, Aug. 2017.

[21] B. Kundu, P. Mohanty, and P. K. Sahoo, "Chapter 2 - Synthesis of 2D heterostructures," in *2D Materials for Electronics, Sensors and Devices* (S. Das, ed.), Nanophotonics, pp. 55–95, Elsevier, Jan. 2023.

[22] P. K. Sahoo, S. Memaran, Y. Xin, L. Balicas, and H. R. Gutiérrez, "One-pot growth of two-dimensional lateral heterostructures via sequential edge-epitaxy," *Nature*, vol. 553, pp. 63–67, Jan. 2018.

[23] P. K. Sahoo, S. Memaran, F. A. Nugera, Y. Xin, T. Díaz Márquez, Z. Lu, W. Zheng, N. D. Zhigadlo, D. Smirnov, L. Balicas, and H. R. Gutiérrez, "Bilayer Lateral Heterostructures of Transition-Metal Dichalcogenides and Their Optoelectronic Response," *ACS Nano*, vol. 13, pp. 12372–12384, Nov. 2019.

[24] P. A. Markeev, E. Najafidehaghani, Z. Gan, K. Sotthewes, A. George, A. Turchanin, and M. P. de Jong, "Energy-Level Alignment at Interfaces between Transition-Metal Dichalcogenide Monolayers and Metal Electrodes Studied with Kelvin Probe Force Microscopy," *The Journal of Physical Chemistry C*, vol. 125, pp. 13551–13559, June 2021.

[25] Y. Guo, D. Liu, and J. Robertson, "3D Behavior of Schottky Barriers of 2D Transition-Metal Dichalcogenides," *ACS Applied Materials & Interfaces*, vol. 7, pp. 25709–25715, Nov. 2015.

[26] Z. Lin, B. R. Carvalho, E. Kahn, R. Lv, R. Rao, H. Terrones, M. A. Pimenta, and M. Terrones, "Defect engineering of two-dimensional transition metal dichalcogenides," *2D Materials*, vol. 3, p. 022002, Apr. 2016.

[27] R. Addou, S. McDonnell, D. Barrera, Z. Guo, A. Azcatl, J. Wang, H. Zhu, C. L. Hinkle, M. Quevedo-Lopez, H. N. Alshareef, L. Colombo, J. W. P. Hsu, and R. M. Wallace, "Impurities and Electronic Property Variations of Natural MoS2 Crystal Surfaces," *ACS nano*, vol. 9, pp. 9124–9133, Sept. 2015.

[28] S. Luo, G. Hao, Y. Fan, L. Kou, C. He, X. Qi, C. Tang, J. Li, K. Huang, and J. Zhong, "Formation of ripples in atomically thin MoS and local strain engineering of electrostatic properties," *Nanotechnology*, vol. 26, p. 105705, Mar. 2015.

[29] P. Zhang, Y. Zhang, Y. Wei, H. Jiang, X. Wang, and Y. Gong, "Contact engineering for two-dimensional semiconductors," *Journal of Semiconductors*, vol. 41, p. 071901, July 2020.

[30] S. Das, H.-Y. Chen, A. V. Penumatcha, and J. Appenzeller, "High performance multilayer MoS2 transistors with scandium contacts," *Nano Letters*, vol. 13, pp. 100–105, Jan. 2013.

[31] X. Zhang, F. Zhang, Y. Wang, D. S. Schulman, T. Zhang, A. Bansal, N. Alem, S. Das, V. H. Crespi, M. Terrones, and J. M. Redwing, "Defect-Controlled Nucleation and Orientation of WSe2 on hBN: A Route to Single-Crystal Epitaxial Monolayers," *ACS Nano*, vol. 13, pp. 3341–3352, Mar. 2019.

[32] Y. Wang, J. C. Kim, Y. Li, K. Y. Ma, S. Hong, M. Kim, H. S. Shin, H. Y. Jeong, and M. Chhowalla, "P-type electrical contacts for 2D transition-metal dichalcogenides," *Nature*, vol. 610, pp. 61–66, Oct. 2022.

[33] C. Li, J. Zhu, W. Du, Y. Huang, H. Xu, Z. Zhai, and G. Zou, "The Photodetectors Based on Lateral Monolayer MoS2/WS2 Heterojunctions," *Nanoscale Research Letters*, vol. 16, pp. 1–9, Dec. 2021.

[34] P. D'Agosta, F. Tumino, V. Russo, A. Li Bassi, and C. S. Casari, "Interface coupling in Au-supported MoS2–WS2 heterobilayers grown by pulsed laser deposition," *Nanoscale*, vol. 15, no. 16, pp. 7493–7501.

[35] A. B. Patel, P. Chauhan, K. Patel, C. K. Sumesh, S. Narayan, K. D. Patel, G. K. Solanki, V. M. Pathak, P. K. Jha, and V. Patel, “Solution-Processed Uniform MoSe2–WSe2 Heterojunction Thin Film on Silicon Substrate for Superior and Tunable Photodetection,” *ACS Sustainable Chemistry & Engineering*, vol. 8, pp. 4809–4817, Mar. 2020.

[36] G. Wang, L. Li, W. Fan, R. Wang, S. Zhou, J.-T. Lü, L. Gan, and T. Zhai, “Interlayer Coupling Induced Infrared Response in WS2/MoS2 Heterostructures Enhanced by Surface Plasmon Resonance,” *Advanced Functional Materials*, vol. 28, no. 22, p. 1800339, 2018.

[37] A. Sumanth, K. L. Ganapathi, M. S. R. Rao, and T. Dixit, “A review on realizing the modern optoelectronic applications through persistent photoconductivity,” *Journal of Physics D: Applied Physics*, vol. 55, p. 393001, July 2022.

[38] S. H. Song, J. M. Kim, and B. S. Yoo, “Use of a persistent photoconductive array in the learning of an optoelectronic neural processor,” *Optics Letters*, vol. 16, pp. 1771–1773, Nov. 1991.

[39] H. J. Queisser and D. E. Theodorou, “Decay kinetics of persistent photoconductivity in semiconductors,” *Physical Review B*, vol. 33, pp. 4027–4033, Mar. 1986.

[40] D. V. Lang and R. A. Logan, “Large-Lattice-Relaxation Model for Persistent Photoconductivity in Compound Semiconductors,” *Physical Review Letters*, vol. 39, pp. 635–639, Sept. 1977.

[41] D. V. Lang, R. A. Logan, and M. Jaros, “Trapping characteristics and a donor-complex model for the persistent-photoconductivity trapping center in Te-doped AlGaAs,” *Physical Review B*, vol. 19, pp. 1015–1030, Jan. 1979.

[42] A. D. Bartolomeo, L. Genovese, T. Foller, F. Giubileo, G. Luongo, L. Croin, S.-J. Liang, L. K. Ang, and M. Schleberger, “Electrical transport and persistent photoconductivity in monolayer MoS2 phototransistors,” *Nanotechnology*, vol. 28, p. 214002, May 2017.

[43] X. Li, M.-W. Lin, A. A. Puretzky, L. Basile, K. Wang, J. C. Idrobo, C. M. Rouleau, D. B. Geohegan, and K. Xiao, “Persistent photoconductivity in two-dimensional Mo1xWxSe2–MoSe2 van der Waals heterojunctions,” *Journal of Materials Research*, vol. 31, pp. 923–930, Apr. 2016.

[44] H. H. Berger, “Models for contacts to planar devices,” *Solid-State Electronics*, vol. 15, pp. 145–158, Feb. 1972.

[45] A. M. Hoque, V. Ramachandra, A. George, E. Najafidehaghani, Z. Gan, R. Mitra, B. Zhao, D. Khokhriakov, A. Turchanin, S. Lara-Avila, S. Kubatkin, and S. P. Dash, “Spin-valley coupling and spin-relaxation anisotropy in all-CVD Graphene-MoS2 van der Waals heterostructure,” *Physical Review Materials*, vol. 7, p. 044005, Apr. 2023.

[46] M. F. Hossen, S. Shendokar, and S. Aravamudhan, “Defects and Defect Engineering of Two-Dimensional Transition Metal Dichalcogenide (2D TMDC) Materials,” *Nanomaterials*, vol. 14, p. 410, Jan. 2024.

[47] D. A. Neamen, *Semiconductor physics and devices: Basic principles.* 4th ed.

[48] A. Ayari, E. Cobas, O. Ogundadegbe, and M. S. Fuhrer, “Realization and electrical characterization of ultrathin crystals of layered transition-metal dichalcogenides,” *Journal of Applied Physics*, vol. 101, p. 014507, Jan. 2007.

[49] M. Bizhani, R. Thorat, W. Poston, T. Wickramasinghe, S. H. Aleithan, and E. Stinaff, "Thermal Annealing Effects on Naturally Contacted Monolayer MoS2," *physica status solidi (b)*, vol. 258, no. 9, p. 2000426, 2021.

[50] R. Ko, D. H. Lee, and H. Yoo, "Annealing and Doping Effects on Transition Metal Dichalcogenides—Based Devices: A Review," *Coatings*, vol. 13, p. 1364, Aug. 2023.

[51] A. Chaves, J. G. Azadani, H. Alsalman, D. R. da Costa, R. Frisenda, A. J. Chaves, S. H. Song, Y. D. Kim, D. He, J. Zhou, A. Castellanos-Gomez, F. M. Peeters, Z. Liu, C. L. Hinkle, S.-H. Oh, P. D. Ye, S. J. Koester, Y. H. Lee, P. Avouris, X. Wang, and T. Low, "Bandgap engineering of two-dimensional semiconductor materials," *npj 2D Materials and Applications*, vol. 4, pp. 1–21, Aug. 2020.

[52] J. Y. Lim, M. Kim, Y. Jeong, K. R. Ko, S. Yu, H. G. Shin, J. Y. Moon, Y. J. Choi, Y. Yi, T. Kim, and S. Im, "Van der Waals junction field effect transistors with both n- and p-channel transition metal dichalcogenides," *npj 2D Materials and Applications*, vol. 2, pp. 1–7, Nov. 2018.

[53] T. Dutta, N. Yadav, Y. Wu, G. J. Cheng, X. Liang, S. Ramakrishna, A. Sbai, R. Gupta, A. Mondal, Z. Hongyu, and A. Yadav, "Electronic properties of 2D materials and their junctions," *Nano Materials Science*, vol. 6, pp. 1–23, Feb. 2024.

[54] Y. S. Ang, L. Cao, and L. K. Ang, "Physics of electron emission and injection in two-dimensional materials: Theory and simulation," *InfoMat*, vol. 3, no. 5, pp. 502–535, 2021.

[55] Y. S. Ang, H. Y. Yang, and L. Ang, "Universal Scaling Laws in Schottky Heterostructures Based on Two-Dimensional Materials," *Physical Review Letters*, vol. 121, p. 056802, Aug. 2018.

[56] S. Conti, D. Neilson, F. M. Peeters, and A. Perali, "Transition Metal Dichalcogenides as Strategy for High Temperature Electron-Hole Superfluidity," *Condensed Matter*, vol. 5, p. 22, Mar. 2020.

[57] D. Somvanshi, S. Kallatt, C. Venkatesh, S. Nair, G. Gupta, J. K. Anthony, D. Karmakar, and K. Majumdar, "Nature of carrier injection in metal/2D semiconductor interface and its implications to the limits of contact resistance," *Physical Review B*, vol. 96, p. 205423, Nov. 2017. arXiv:1703.00671 [cond-mat].

[58] A. Grillo and A. Di Bartolomeo, "A Current–Voltage Model for Double Schottky Barrier Devices," *Advanced Electronic Materials*, vol. 7, no. 2, p. 2000979, 2021.

[59] J. A. Cloninger, R. Harris, K. L. Haley, R. M. Sterbentz, T. Taniguchi, K. Watanabe, and J. O. Island, "A back-to-back diode model applied to MoS2 van der Waals Schottky diodes," Feb. 2024. arXiv:2402.03611 [cond-mat].

[60] J. Osvald, "Back-to-back connected asymmetric Schottky diodes with series resistance as a single diode," *physica status solidi (a)*, vol. 212, no. 12, pp. 2754–2758, 2015.

[61] T. Kim, S. Fan, S. Lee, M.-K. Joo, and Y. H. Lee, "High-mobility junction field-effect transistor via graphene/MoS2 heterointerface," *Scientific Reports*, vol. 10, p. 13101, Aug. 2020.

[62] A. Di Bartolomeo, A. Grillo, F. Urban, L. Iemmo, F. Giubileo, G. Luongo, G. Amato, L. Croin, L. Sun, S.-J. Liang, and L. K. Ang, "Asymmetric Schottky Contacts in Bilayer MoS2 Field Effect Transistors," *Advanced Functional Materials*, vol. 28, no. 28, p. 1800657, 2018.

[63] H. Zhong, R. Quhe, Y. Wang, Z. Ni, M. Ye, Z. Song, Y. Pan, J. Yang, L. Yang, M. Lei, J. Shi, and J. Lu, "Interfacial Properties of Monolayer and Bilayer MoS2 Contacts with Metals: Beyond the Energy Band Calculations," *Scientific Reports*, vol. 6, p. 21786, Mar. 2016.

[64] X. Liu, M. S. Choi, E. Hwang, W. J. Yoo, and J. Sun, "Fermi Level Pinning Dependent 2D Semiconductor Devices: Challenges and Prospects," *Advanced Materials*, vol. 34, no. 15, p. 2108425, 2022.

[65] M. Buscema, J. O. Island, D. J. Groenendijk, S. I. Blanter, G. A. Steele, H. S. J. v. d. Zant, and A. Castellanos-Gomez, "Photocurrent generation with two-dimensional van der Waals semiconductors," *Chemical Society Reviews*, vol. 44, pp. 3691–3718, May 2015.

[66] M. Long, P. Wang, H. Fang, and W. Hu, "Progress, Challenges, and Opportunities for 2D Material Based Photodetectors," *Advanced Functional Materials*, vol. 29, no. 19, p. 1803807, 2019.

[67] I. M. Datye, A. J. Gabourie, C. D. English, K. K. H. Smithe, C. J. McClellan, N. C. Wang, and E. Pop, "Reduction of hysteresis in MoS2 transistors using pulsed voltage measurements," *2D Materials*, vol. 6, p. 011004, Oct. 2018.

[68] Y. Takanashi, K. Takahata, and Y. Muramoto, "Characteristics of InAlAs/InGaAs high-electron-mobility transistors under illumination with modulated light," *IEEE Transactions on Electron Devices*, vol. 46, pp. 2271–2277, Dec. 1999.

[69] E. A. Bahaa, "Semiconductor Photon Detectors," in *Fundamentals of Photonics*, pp. 644–695, John Wiley & Sons, Ltd, 1991.

[70] M. Bernardi, M. Palummo, and J. C. Grossman, "Extraordinary Sunlight Absorption and One Nanometer Thick Photovoltaics Using Two-Dimensional Monolayer Materials," *Nano Letters*, vol. 13, pp. 3664–3670, Aug. 2013.

[71] C.-C. Wu, D. Jariwala, V. K. Sangwan, T. J. Marks, M. C. Hersam, and L. J. Lauhon, "Elucidating the Photoresponse of Ultrathin MoS2 Field-Effect Transistors by Scanning Photocurrent Microscopy," *The Journal of Physical Chemistry Letters*, vol. 4, pp. 2508–2513, Aug. 2013.

[72] Y. Fan, Y. Zhou, X. Wang, H. Tan, Y. Rong, and J. H. Warner, "Photoinduced Schottky Barrier Lowering in 2D Monolayer WS2 Photodetectors," *Advanced Optical Materials*, vol. 4, no. 10, pp. 1573–1581, 2016.

[73] T. Sugeta, T. Urisu, S. Sakata, and Y. Mizushima, "Metal-Semiconductor-Metal Photodetector for High-Speed Optoelectronic Circuits," *Japanese Journal of Applied Physics*, vol. 19, p. 459, Jan. 1980.

[74] C.-H. Chen, "AlInGaN 310 nm ultraviolet metal-insulator-semiconductor sensors with photo-chemical-vapor-deposition SiO2 cap layers," *Optical Review*, vol. 16, pp. 371–374, May 2009.

[75] O. Katz, V. Garber, B. Meyler, G. Bahir, and J. Salzman, "Gain mechanism in GaN Schottky ultraviolet detectors," *Applied Physics Letters*, vol. 79, pp. 1417–1419, Sept. 2001.

[76] J. Zhou, Y. Gu, Y. Hu, W. Mai, P.-H. Yeh, G. Bao, A. K. Sood, D. L. Polla, and Z. L. Wang, "Gigantic enhancement in response and reset time of ZnO UV nanosensor by utilizing Schottky contact and surface functionalization," *Applied Physics Letters*, vol. 94, p. 191103, May 2009.

[77] J. Hao, S. A. Studenikin, and M. Cocivera, "Transient photoconductivity properties of tungsten oxide thin films prepared by spray pyrolysis," *Journal of Applied Physics*, vol. 90, pp. 5064–5069, Nov. 2001.

[78] J. S. Jie, W. J. Zhang, Y. Jiang, X. M. Meng, Y. Q. Li, and S. T. Lee, "Photoconductive Characteristics of Single-Crystal CdS Nanoribbons," *Nano Letters*, vol. 6, pp. 1887–1892, Sept. 2006.

[79] S. A. Studenikin and M. Cocivera, "Time-resolved luminescence and photoconductivity of polycrystalline ZnO films," *Journal of Applied Physics*, vol. 91, pp. 5060–5065, Apr. 2002.

[80] S. Ghatak, A. N. Pal, and A. Ghosh, "Nature of Electronic States in Atomically Thin MoS2 Field-Effect Transistors," *ACS Nano*, vol. 5, pp. 7707–7712, Oct. 2011.

[81] C.-P. Lu, G. Li, J. Mao, L.-M. Wang, and E. Y. Andrei, "Bandgap, mid-gap states, and gating effects in MoS2," *Nano Letters*, vol. 14, pp. 4628–4633, Aug. 2014.

[82] W. H. Chae, J. D. Cain, E. D. Hanson, A. A. Murthy, and V. P. Dravid, "Substrate-induced strain and charge doping in CVD-grown monolayer MoS2," *Applied Physics Letters*, vol. 111, p. 143106, Oct. 2017.

[83] P. Johari and V. B. Shenoy, "Tuning the Electronic Properties of Semiconducting Transition Metal Dichalcogenides by Applying Mechanical Strains," *ACS Nano*, vol. 6, pp. 5449–5456, June 2012.

A

Water assisted one pot CVD growth of 2D TMD LHS

Water assisted one pot synthesis method is used to fabricate the TMD lateral heterostructure. In this growth strategy, a heterogenous mixture of MoX_2 and WX_2 (X= S, Se) is used as a source precursor and only the type of carrier gas type is controlled to attain the selective TMD domain growth [22]. In this master's thesis, a bilayer MoS_2/WS_2 grown using this method is used to fabricate the FET. The growth substrate temperature is maintained in the range of 750°C to 800°C and the carrier gas is maintained at 1060°C.

For the initial growth of MoX_2 domains, N_2 along with water vapour is used as a carrier gas to promote the vaporization of MoX_2 precursor. At high temperature (1060°C), the water vapour oxidises the MoX_2 precursor to MoO_2 (reaction A.1) which is transported to the growth substrate. At the substrate, the MoO_2 interacts with H_2X and forms MoX_2 domains (reaction A.2).

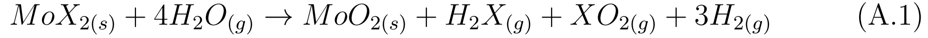

$$MoX_{2(s)} + 4H_2O_{(g)} \rightarrow MoO_{2(s)} + H_2X_{(g)} + XO_{2(g)} + 3H_{2(g)} \quad \text{(A.1)}$$

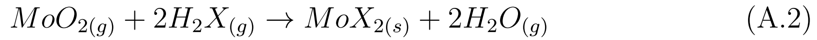

$$MoO_{2(g)} + 2H_2X_{(g)} \rightarrow MoX_{2(s)} + 2H_2O_{(g)} \quad \text{(A.2)}$$

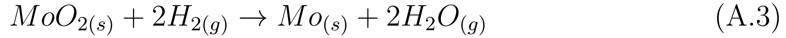

$$MoO_{2(s)} + 2H_{2(g)} \rightarrow Mo_{(s)} + 2H_2O_{(g)} \quad \text{(A.3)}$$

Before growing the next TMD domain (WX_2), the growth of MoX_2 is terminated by switching the carrier gas to Ar/H_2 (5). The H_2 aids in the rapid reduction of MoO_2 (reaction A.3). On the other hand, WX_2 precursors interact with H2 and H_2O to form different W suboxides such as WO_2, $W_{18}O_{18}$, $W_{20}O_{58}$. But, due to the poor evaporation rate, these suboxides do not take part in the growth process. When the carrier gas is switched from H_2O to H_2, high index W suboxides undergoes a phase transition to low index suboxides by interacting with H_2 which subsequently evaporates and sublimates to form WX_2 domains (reaction A.4 and A.5).

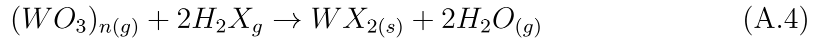

$$(WO_3)_{n(g)} + 2H_2X_g \rightarrow WX_{2(s)} + 2H_2O_{(g)} \quad \text{(A.4)}$$

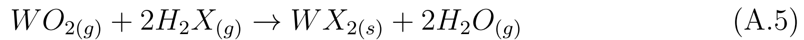

$$WO_{2(g)} + 2H_2X_{(g)} \rightarrow WX_{2(s)} + 2H_2O_{(g)} \quad \text{(A.5)}$$

Figure A.1 illustrates the one pot growth mechanism of MoS_2/WS_2 LHS. Multiple heterojunctions are obtained by sequentially changing the carrier gases between N_2

+ H_2O and Ar + H_2. The monolayer and bilayer LHS are obtained by controlling the growth temperature. High temperature favours vertical epitaxial growth and low temperature promotes monolayer growth. The bilayer MoS_2/WS_2 LHS are synthesised by placing the growth substrate closer to the source where the temperature is > 800^oC. Figure A.2a shows the relative kinetic coefficients of detachment and attachment of adatoms on the edges of the developing TMD layers. Figure A.2b shows the optical image of the fabricated Bilayer MoS_2-WS_2 having faceted hexagonal geometry.

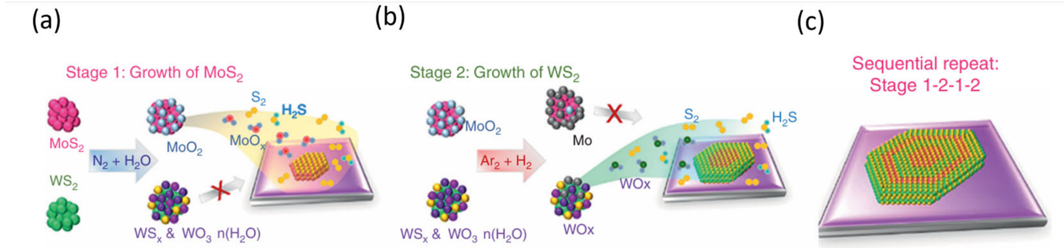

Figure A.1: Schematic representation of the growth mechanism of MoS_2/WS_2 lateral heterostructure (a) N_2 and H_2O promotes selective evaporation of Mo related precursors which results in the growth of MoS_2 (b) Switching the carrier gas to Ar and H_2, promotes the growth of WS_2 while terminating the MoS_2 growth. (c) Formation of multijunction by sequential exchange of carrier gas. This figure is adapted from [23]

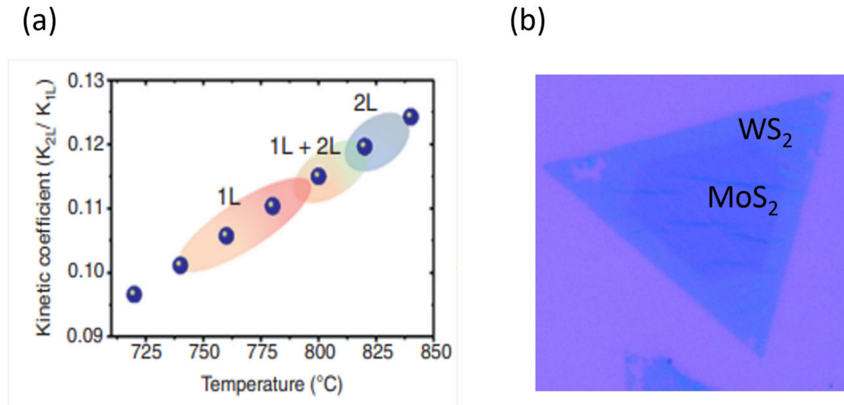

Figure A.2: : (a) Relative kinetic coefficient (K_{n+}/K_{n-}) as a function of growth temperature, combination of monolayer and bilayer LHS are formed at higher temperature (>800^oC) (b) Optical image of Bilayer MoS_2-WS_2 having faceted hexagonal geometry after PMMA assisted transfer.

B

Fabrication

In this section the process flow of the device fabrication is discussed. Cleanroom facilities at Myfab Chalmers is used to fabricate the devices. Figure B.1 explains the fabrication process with schematic diagrams.

1. PMMA transfer method

   (a) The PMMA is spin coated on the growth substrate at 700 rpm at an acceleration of 300 cm^2/s^2 for 60 sec. The sample is prebaked at 60^oC for 10 min.
   (b) The PMMA-coated growth substrate is immersed in H_2O. The capillary action draws the water to the substrate/PMMA interface and detaches the hydrophobic PMMA/TMD from the growth substrate. The detached PMMA/TMD flakes float on the surface of the water.
   (c) The PMMA/TMD film is fished out of the water and transferred to the target substrate (SiO_2/Si).
   (d) The PMMA resist is removed from the target substrate in an acetone bath at 60^oC for 5 min and IPA rinse, followed by N_2 blow dry.

2. Channel patterning using electron beam lithography and reactive plasma etching

   (a) Spin-coated MMA EL8 at 6000 rpm for 60 sec followed by prebaking at 150^oC for 10 min. Prebake is used to evaporate the solvent from the resist. Prebaking improves the adhesion, uniformity and etch resistance of the resist.
   (b) Spin-coated ARP at 6000 rpm for 60 sec followed by prebaking at 135^oC for 7 min. Double-layer resist is used to avoid undercut.
   (c) Exposed the sample in e-beam current.
   (d) The sample is developed in n amyl acetate for 45 sec, and 1:1 MIBK: IPA for 1 min 15 sec, followed by acetone and IPA rinse.
   (e) The exposed TMDs are etched away using CHF_3/Ar for 40 sec followed by O_2 stripping for 20 sec.
   (f) The resist is removed in an acetone bath for 5min at 60^oC followed by IPA rinse and N_2 blow dry.

3. Contact electrode deposition using electron beam lithography and electron beam evaporation

    (a) Spin coated MMA EL8 at 6000 rpm/3000 acc for 60 sec followed by prebaking at 135°C for 8 min and ARP at 6000 rpm and 300 acc for 60 sec, baked at 135°C for 7 min.
    (b) Exposed the sample in e-beam current.
    (c) The sample is developed in n- amyl acetate for 45 sec, and 1:1 MIBK: IPA for 1 min 15 sec, followed by IPA rinse.
    (d) Electron beam evaporator- Lesker PVD 225 is used for contact electrode deposition. The deposition pressure is maintained at 10-7 Torr.
    (e) The metal and the resist are lifted off in an acetone bath at 60°C for 5 min, followed by IPA rinse.

4. Annealing

    (a) The sample is annealed at 180°C for 2 hrs in Ar/H_2 environment.

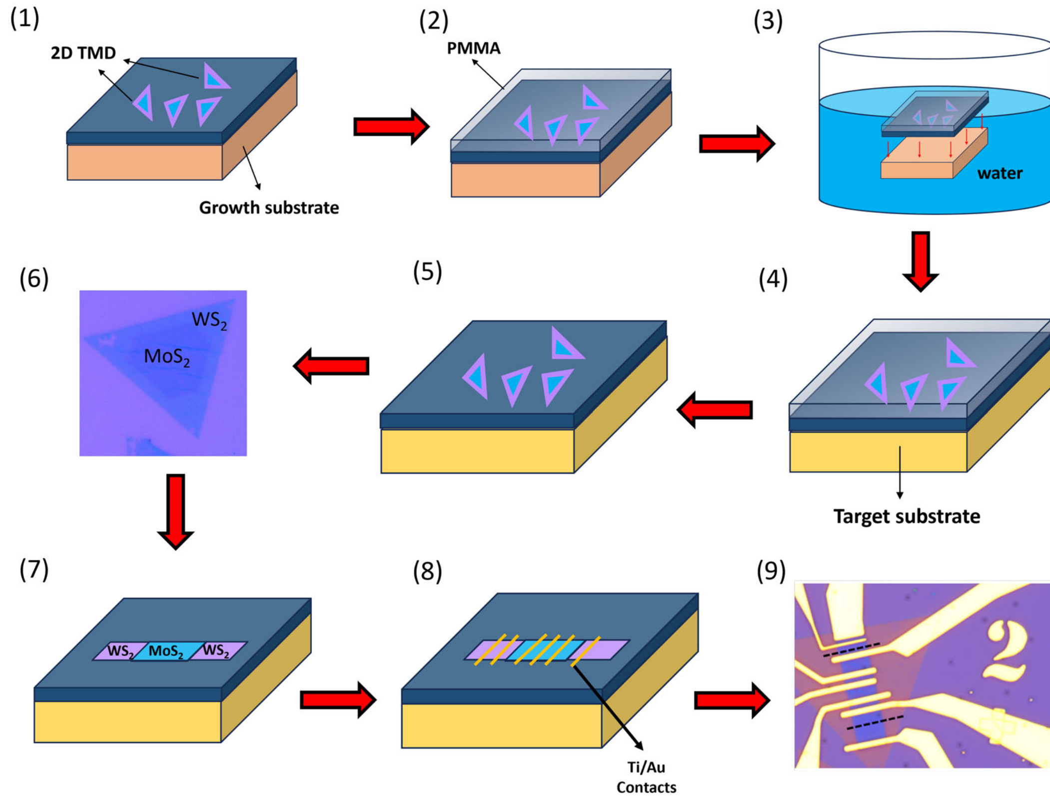

Figure B.1: Step by step process flow for the fabrication of lateral heterostructure TMD FET: (1) Schematic diagram of as-grown lateral MoS_2-WS_2 heterostructure on the growth substrate. (2) PMMA is spin-coated on the growth substrate. (3) The PMMA-coated growth substrate is immersed in water. (4) PMMA/TMD film is fished out of the water and transferred to the target substrate. (5) PMMA is removed from the target substrate using acetone and IPA. (6) Optical image of the transferred MoS_2-WS_2 LHS. The dark contrast region corresponds to MoS_2 and the bright contrast region corresponds to WS_2. (7) The channel is patterned using EBL and CHF_3/Ar etching. (8) Ti/Au is deposited using an e-beam evaporator. (9) Optical image of the fabricated device. The dotted black line is the MoS_2-WS_2 heterojunction.

C

Supplemenatry

C.1 Supplementary MoS_2 and WS_2 results

Figure C.1 shows the electrical characterization of MoS_2 and WS_2. Figure C.1 (a) shows the two point and four point probe output characteristics of MoS_2. In 2PP measurements, the voltages and currents are applied and measured at the same terminals. The presence of contact resistance in the 2PP measurements often leads to significant errors in the parameters extracted from the transfer and output characteristics curves. The 4-point probe (4PP) method, which avoids the effect of contact resistances is preferred for accurate measurements of parameters such as channel sheet resistance, field effect mobility, and threshold voltage.

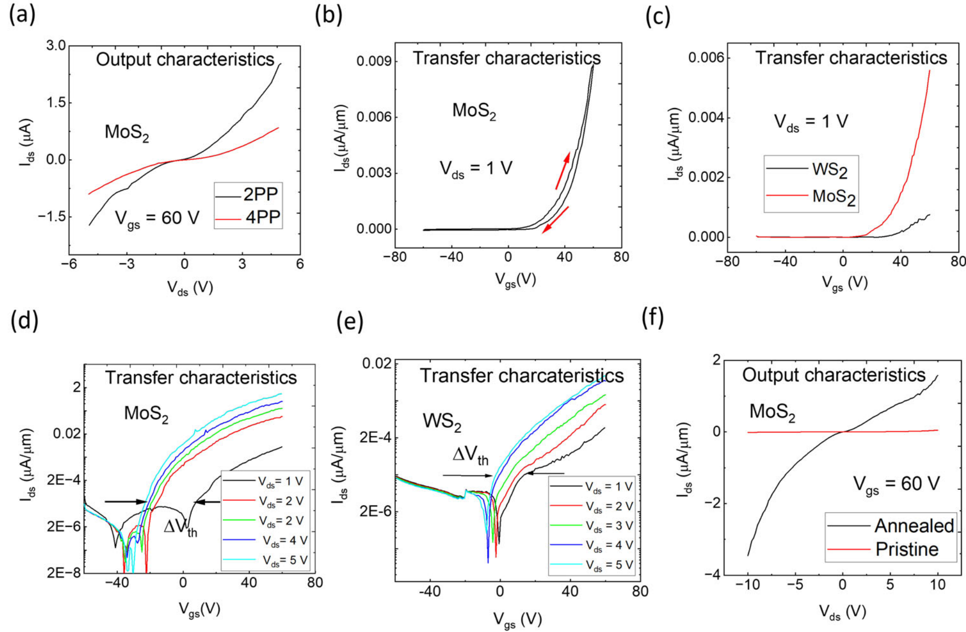

Figure C.1: Electrical characterization of MoS_2 and WS_2: (a) Comparison between two-point probe (2PP) and four-point probe (4PP) of output characteristics curve of MoS_2. (b) Transfer characteristics curve of MoS_2 at V_{ds} = 1V with forward and reverse sweep showing the presence of hysteresis. (c) Transfer characteristics curve of MoS_2 and WS_2 at V_{ds} = 1V. The threshold voltage (V_T) of MoS_2 is lower than that of WS_2. (d), (e) Transfer curve of MoS_2 and WS_2 for different V_{ds} in logarithmic scale. The decrease in V_T with the increase in V_{ds} confirms the presence of DIBL. (f) Comparison between annealed and pristine MoS_2 sample.

Figure C.1 (b) shows the observed hysteresis in the transfer characteristic curve of MoS_2. The difference in the threshold voltage between the forward and reverse voltage sweep is defined as the hysteresis. Hysteresis arises due to the presence of trapped charges at the SiO_2 – TMD interface and on the surface of the TMDs. When the fermi level moves towards the valence band edge during the reverse sweep, the traps above the fermi level get emptied and become positively charged which causes the observed negative shift in V_T. During the forward sweep, as the fermi level moves closer to the conduction band edge, the trap states that are presented below the fermi level get occupied by electrons and become neutralised, resulting in a positive V_T shift. The absence of the device encapsulation (eg, with Al_2O_3) in our fabricated device has resulted in large hysteresis. Typically, the hysteresis depends on environmental conditions, voltage sweep rate, sweep direction and sweep range.

C.2 Supplementary MoS_2-WS_2 heterojunction results

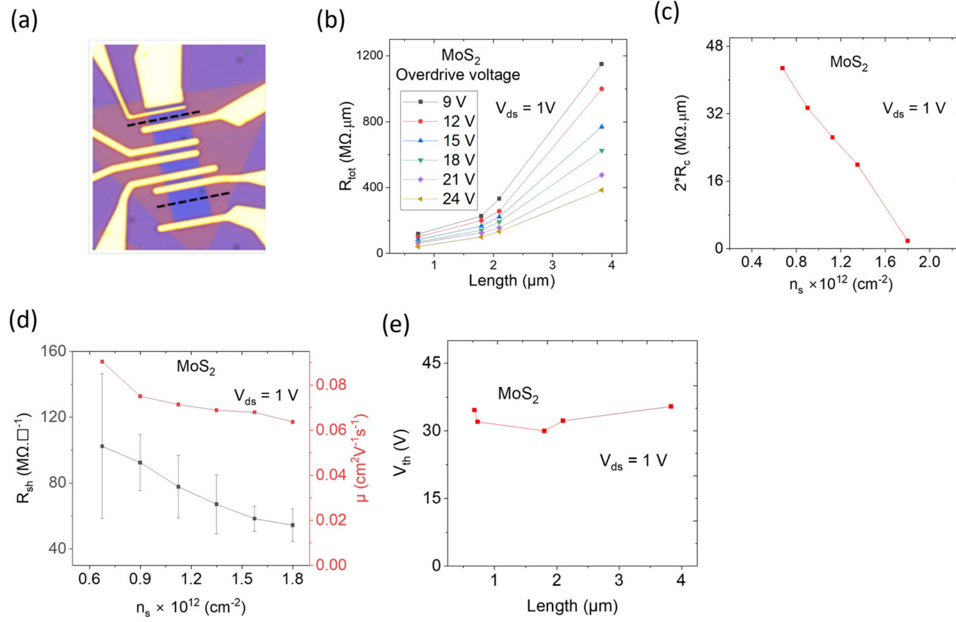

Figure C.2: Transfer length method (TLM) analysis of MoS_2: (a) Optical image of the fabricated MoS_2-WS_2 lateral heterostructure with TLM structure on MoS_2. (b) Total resistance (R_{tot} vs channel length (L_{ch}) for different overdrive voltages at V_{ds} = 1V. The contact resistance ($2R_C$) and channel sheet resistance (R_{Sh}) are extracted from the y-intercept and the slope respectively. (c) Contact resistance ($2R_C$) as a function of charge carrier density (n_s). (d) Sheet resistance ($2R_{Sh}$) as a function of charge carrier density (n_s). (e) Plot showing the dependence of the extracted threshold voltage (V_T) of MoS_2 on L_{ch}

.

Figure C.2 shows the transfer length method (TLM) analysis of Mos_2. We used the TLM structure to extract the contact resistances (R_c) and sheet resistances (R_{sh}) of MoS_2. The channel length is varied from 0.75 μm to 4 μm. Figure C.2 (b) shows the plot between the total resistance (R_{tot}) and channel length (L_{ch}) for different overdrive voltages (V_{Ov}). The contact resistances and sheet resistances are extracted from the y-intercept and slope of the plot respectively. The calculated R_c and R_{sh} are in the range of M$\Omega.\mu$m. The decrease in contact resistances with the increase in carrier density (n_s) as shown in the figure C.2(c) confirms the presence of Schottky barrier contacts. As the carrier density increases, the width of the Schottky decreases which enhances the tunnelling current. The carrier density (n_s) is calculated from the threshold voltage using the expression $n_s = (C_{ins}.V_{Ov})/q$. The calculated conductivity mobility (μ_{con}) using the expression $\mu_{con} = 1/(q.n_s.R_{sh})$ is around 0.06 $\mu cm^2V^{-1}s^{-1}$.

C.3 Supplementary SBH extraction results

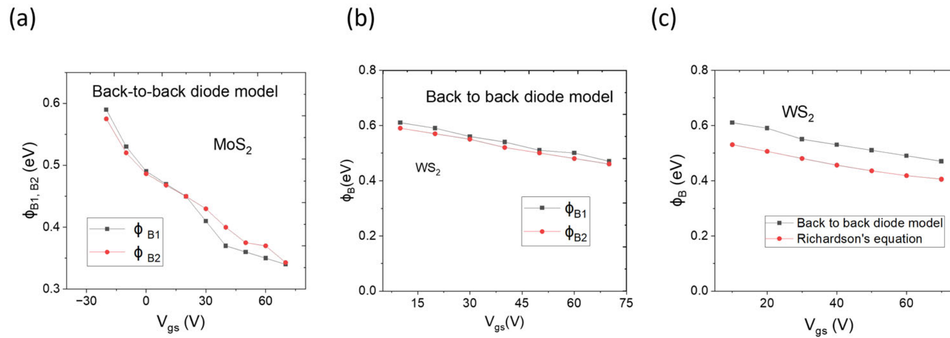

Figure C.3: Extraction of Schottky barrier height (SBH):(a), (b) Comparison of the extracted SBH at source and drain contacts for MoS_2 and WS_2. No significant difference in SBH is observed at source and drain contacts. (c) Dependence of SBH on gate voltage V_{gs}.

Figure C.3(a) and C.3(b) shows the comparison of Schottky barrier height extracted from the back-to-back diode model at the source and drain contacts for MoS_2 and WS_2. It is evident from the plots that there is no significant difference between ϕ_{B1} and ϕ_{B2}. Therefore, the fermi level is pinned at almost same energy level. Figure C.3(c) compares the SBH extracted from Richardson's equation and back-to-back diode model. Since there is no thermionic-tunnelling transition, we couldn't extract the actual SBH of WS_2-Ti contacts.

C.4 Supplementary photoresponse results

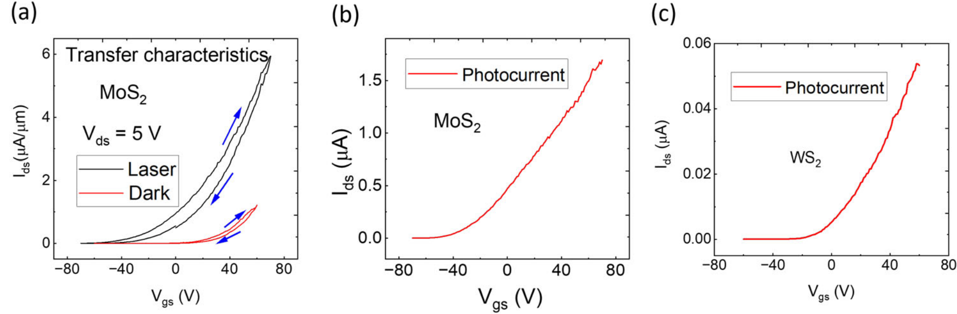

Figure C.4: Optoelectronic characterization of MoS_2 and WS_2: (a) Comparison of transfer characteristic curve of MoS_2 under laser illumination with dark condition at V_{ds} = 5 V. A significant increase in hysteresis is observed under illumination. (b), (c) Plot showing the extracted photocurrent (I_{Ph}) for MoS_2 and WS_2 respectively. The photocurrent is obtained by subtracting the dark current from the current under laser illumination. The photocurrent increases with the gate voltage.

Figure C.4 (a) shows the full sweep transfer curve of MoS_2 under LED laser and under dark condition. The prominent increase in hysteresis is due to the trapped charged carrier upon illumination. Figure C.4(b) and C.4(c) shows the dependence of the photocurrent on gate voltage.

C.5 Supplementary table

	MoS_2		
	Pristine	**Annealed**	**Laser illuminated**
$\mathbf{I}_{max}$ ($\mu A/\mu m$)	1.1 $\times 10^{-2}$	0.14	0.38
$\mathbf{I}_{min}$ ($\mu A/\mu m$	1.7 $\times 10^{-7}$	2.4 $\times 10^{-6}$	1.4 $\times 10^{-9}$
$\mathbf{I}_{max}$ / $\mathbf{I}_{min}$	6.4 $\times 10^{3}$	5.7 $\times 10^{4}$	2.7 $\times 10^{8}$
SS (V/dec)	2	5.7	1.9
$\mathbf{V}_T$	24	6.4	-20
$\mu(cm^{-2}V^{-1}s^{-1})$	0.055 $\pm$ 0.026	0.45 $\pm$ 0.08	0.7 $\pm$ 0.13
DIBL (V/V)	4.2	1.2	

Table C.1: Basic transistor parameters of MoS_2 in pristine, annealed and laser illuminated conditions

MoS_2-WS_2 Heterojunction			
	Pristine	**Annealed**	**Laser illuminated**
$\mathbf{I}_{max}$ $(\mu A/\mu m)$	1×10^{-2}	0.047	0.1
$\mathbf{I}_{min}$ $(\mu A/\mu m$	0.35×10^{-5}	2×10^{-6}	2×10^{-7}
$\mathbf{I}_{max}$ / $\mathbf{I}_{min}$	2857×10^{3}	2.35×10^{4}	5×10^{5}
SS (V/dec)	4.44	2.45	1.29
$\mathbf{V}_T$	29	20	11.5
$\mu(cm^{-2}V^{-1}s^{-1})$	0.13 ± 0.03	0.47 ± 0.09	0.62 ± 0.14

Table C.2: Basic transistor parameters of MoS_2-WS_2 Heterojunction in pristine, annealed and laser illuminated conditions

WS_2		
	Pristine	**Laser illuminated**
$\mathbf{I}_{max}$ $(\mu A/\mu m)$	7.4×10^{-4}	0.012
$\mathbf{I}_{min}$ $(\mu A/\mu m$	3×10^{-6}	4×10^{-7}
$\mathbf{I}_{max}$ / $\mathbf{I}_{min}$	246×10^{3}	3×10^{4}
SS (V/dec)	3	3
$\mathbf{V}_T$	34.33	13
$\mu(cm^{-2}V^{-1}s^{-1})$	0.001 ± 0.03	0.62 ± 0.004

Table C.3: Basic transistor parameters of WS_2 in pristine, annealed and laser illuminated conditions

Table C.1, C.2, and C.3 shows the basic transistor parameters of MoS_2, WS_2 and MoS_2-WS_2 Heterojunction in pristine, annealed and under laser illumination conditions. For The annealing has improved almost all the parameters. We saw a significant improvement in mobility, DIBL, and I_{max} / I_{min} ratio. Illuminating the sample with a green LED laser further enhanced the transistor properties.

DEPARTMENT OF SOME SUBJECT OR TECHNOLOGY
CHALMERS UNIVERSITY OF TECHNOLOGY
Gothenburg, Sweden
www.chalmers.se

CHALMERS
UNIVERSITY OF TECHNOLOGY